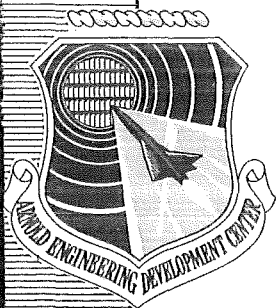# SUMMARY REPORT ON AERODYNAMIC CHARACTERISTICS OF STANDARD MODELS HB-1 AND HB-2

By   AD 602 769

J. Don Gray

von Kármán Gas Dynamics Facility

ARO, Inc.

TECHNICAL DOCUMENTARY REPORT NO. AEDC-TDR-64-137

July 1964

Program Element 65402034

ARNOLD ENGINEERING DEVELOPMENT CENTER

AIR FORCE SYSTEMS COMMAND

UNITED STATES AIR FORCE

NOTICES

SUMMARY REPORT ON AERODYNAMIC CHARACTERISTICS OF STANDARD MODELS HB-1 AND HB-2

By

J. Don Gray

von Kármán Gas Dynamics Facility

ARO, Inc.

a subsidiary of Sverdrup and Parcel, Inc.

ABSTRACT

All available test data on the standard hypersonic ballistic correlation models, HB-1 and HB-2, have been examined to establish reference characteristics for use in the correlation of experimental results among the various aerodynamic facilities. The data presented are comprised primarily of static stability and zero-lift forebody axial-force coefficient results at Mach numbers from about 1.5 to 20 for a Reynolds number range from 0.01 to 2.7 x 10^6 based on centerbody diameter. Selected pressure distribution, dynamic stability, and heat-transfer data are included. Comparisons of data from various test facilities show excellent correlation in spite of the appreciable Reynolds number dependence of test results for model HB-2 with natural boundary-layer transition.

PUBLICATION REVIEW

This report has been reviewed and publication is approved.

Darreld K. Calkins
Major, USAF
AF Representative, VKF
DCS/Test

Jean A. Jack
Colonel, USAF
DCS/Test

CONTENTS

TABLE

ILLUSTRATIONS

NOMENCLATURE

A	Reference area, $\pi d^2/4$, in.^{2}
A_b	Base area, in.^{2}
C_∞	Chapman-Rubesin constant, $\mu_w T_\infty / \mu_\infty T_w$
C_A	Zero-lift forebody axial-force coefficient, $(C_{A_t} - C_{A_b})$
C_{A_b}	Zero-lift base axial-force coefficient, $C_{p_b}(A_b/A)$
C_{A_t}	Total zero-lift axial-force coefficient, $\dfrac{\text{total axial force}}{q_\infty A}$
C_m	Pitching-moment coefficient (reference at 1.95d from nose), $\dfrac{\text{pitching moment}}{q_\infty A d}$
C_{m_q}	Damping-in-pitch derivative, $\partial C_m / \partial (qd/2V_\infty)$, 1/rad
$C_{m_{\dot{\alpha}}}$	Damping-in-pitch derivative, $\partial C_m / \partial (\dot{\alpha}d/2V_\infty)$, 1/rad
C_N	Normal-force coefficient, $\dfrac{\text{normal force}}{q_\infty A}$
C_{N_α}	Slope of normal-force curve, $\left(\partial C_N / \partial \alpha\right)_{\alpha = 0}$
C_p	Pressure coefficient, $(p - p_\infty)/q_\infty$
C_{p_b}	Base pressure coefficient $(p_b - p_\infty)/q_\infty$
c_A	Local axial-force coefficient, $(2/A) \int_0^\pi C_p r \tan \sigma \, d\phi$, 1/in.
c_N	Local normal-force coefficient, $(2/A) \int_0^\pi C_p r \cos \phi \, d\phi$, 1/in.
D	Sting diameter at model base, in.
d	Reference centerbody diameter (see Fig. 1), in.
L	Length of sting of constant diameter, D, in.
ℓ	Overall model length (4.9d), in.
M_∞	Free-stream Mach number
p	Surface pressure, psia
p_∞	Free-stream pressure, psia
p_b	Base pressure, psia

$p_o{}'$	Model stagnation pressure, psia
q	Pitching velocity, rad/sec
q_∞	Free-stream dynamic pressure, $(\gamma/2)\, p_\infty\, M_\infty^2$, psia
$q/q_o{}'$	Heat-transfer rate relative to model stagnation point heat-transfer rate
Re_d	Reynolds number based on centerbody diameter and free-stream conditions
R_N	Blunted nose radius (0.3d), in.
r	Model radius, in.
S	Wetted length, in.
T_∞	Free-stream temperature, °R
T_w	Wall temperature, °R
V_∞	Free-stream velocity, ft/sec
$\overline{V}_\infty$	Viscous parameter, $M_\infty \sqrt{C_\infty}/\sqrt{Re_d}$
x	Axial distance, in.
x_{cp}/ℓ	Center of pressure, $\left[1.95 - \left(dC_m/dC_N\right)_{\alpha=0}\right] d/\ell$
α	Angle of attack, deg
$\dot{\alpha}$	Time rate-of-change of α, rad/sec
β	Sting windshield half-angle, deg
γ	Ratio of specific heats
θ	Angular displacement, deg
μ_∞	Viscosity of air evaluated at free-stream temperature, lb-sec/ft^2
μ_w	Viscosity of air evaluated at wall temperature, lb-sec/ft^2
σ	Local surface inclination, deg
ϕ	Circumferential position, deg
ω	Angular frequency, rad/sec

1.0 INTRODUCTION

The necessity for a standard for the evaluation of data obtained in aerodynamic test facilities is well recognized. Such a standard may be established through the use of identical calibration models in the greatest number of test facilities.

Through an appreciation of the many fundamental factors involved and an awareness of the characteristics of the instrumentation used, a realistic confidence in the validity of test data may be then established. The Advisory Group for Aeronautical Research and Development (AGARD) calibration models are well-known examples of the utility of this approach (Ref. 1).

The desire for a ballistic correlation model was first voiced at the joint meeting of AGARD and STA (Supersonic Tunnel Association) held in France during September 1959, and the initiative for selecting a suitable configuration was assumed by Lukasiewicz of the von Kármán Gas Dynamics Facility (VKF), Arnold Engineering Development Center (AEDC), Air Force Systems Command (AFSC). This resulted in adoption by the STA, in March 1960, of two hypervelocity ballistic model configurations, designated HB-1 and HB-2 (Fig. 1a), which consisted of a blunt cone-cylinder with and without a flare. The latter shape was included to provide a model that would be less sensitive to viscous effects and that would also aid in the evaluation of these effects. A model support sting geometry was also specified as to the maximum diameter and minimum length necessary to provide turbulent base pressure data essentially free of interference (Fig. 1b). These configurations were also submitted for the consideration of the AGARD Fluid Dynamics Panel; at its July 1963 meeting this panel expressed interest in the addition of these models to the AGARD series of standard models, pending review of the already available data on shapes HB-1 and HB-2.

Since the publication of Ref. 2, some additional tests with Models HB-1 and HB-2 have been conducted at the VKF as well as by other organizations. It appears, therefore, that a diverse enough sampling of test measurments has become available to justify a comparison of data. To date, other organizations have tested only the HB-2 configuration with the predominant emphasis being on force measurements.

In particular, the new data consist of force measurements in the 12-in. hypersonic tunnel (Gas Dynamic Wind Tunnel, Hypersonic (E)) and

---

50-in. hypervelocity tunnel (Gas Dynamic Wind Tunnel, Hypersonic (H))
and selected pressure measurements in the 40-in. supersonic tun-
nel (Gas Dynamic Wind Tunnel, Supersonic (A)), the 50-in. hypersonic
Tunnel B, and Tunnel H of the VKF. Data from other organizations con-
sist notably of force results from ONERA in France (Ref. 3), as well as
the Sandia Corp. (unpublished) and RARDE (Ref. 4). Some pressure
distribution results were obtained by the Douglas Aerophysics Labora-
tory (DAL) (Ref. 5) as well as ONERA. In addition, some VKF dynamic
stability measurements at supersonic speeds and heat-transfer data at
Mach 18 are also included. Pertinent details of the test conditions may
be found in Table 1.

2.0 TEST EQUIPMENT

Both configurations are axisymmetric, blunted cone-cylinders
distinguishable by the addition of a flare to the HB-1 model to yield the
HB-2 model. The geometry of these shapes is detailed in Fig. 1a, and
it may be noted that the junctures of the nose and flare with the cylinder
are made by smooth radius fairings. As a matter of interest, the
tangency locations for the various sections of the HB-2 configuration are
given below:

Tangency Locations	
Section	x/ℓ
Hemisphere-Cone	0.0353
Cone-Shoulder	0.1064
Shoulder-Cylinder	0.167
Cylinder-Radius	0.583
Radius-Flare	0.725

As shown in Table 1, many model sizes have been tested, and it is
believed that all conform to the geometry shown in Fig. 1a. Obviously
there are small variations to be expected among the models; however,
it is considered that they are the usual fabrication tolerances and thus
should be a negligible source of discrepancies because of the blunt nose.

All test models were supported by a sting, the geometry of which was
a variable among the various tests, as detailed also in Table 1. The
sting proposed by the STA (Fig. 1b) was specified to have a constant diam-
eter no more than 0.3d for a length of at least 3.0d with a windshield of

20-deg half-angle in order to ensure negligible interference on the base pressure for turbulent flow.

Only test data for which the model was "smooth" are presented; thus, transition location was freely determined by the test facility and model conditions. Only the French (Ref. 3) have investigated the effect of roughness to fix transition; these data are not included herein.

All of these test results were obtained in the wind tunnels briefly described in Table 1. More information on the tunnel characteristics may be found in the references cited.

Inasmuch as diverse facilities are involved in the comparisons to be made, any quotations regarding measurement precision are considered of little value, especially since the basic data required are generally unavailable. It is indeed unfortunate that no widely accepted and common method exists for evaluating data precision as applied to wind-tunnel testing. In certain cases where deviations are clearly related to precision, they will be so noted in the discussion. Otherwise, it is considered that precision is only one of many indeterminate values being judged by the comparisons.

3.0 RESULTS AND DISCUSSION

3.1 FORCE MEASUREMENTS

The normal-force and pitching-moment coefficient characteristics of model HB-1 are shown in Figs. 2 and 3. At most Mach numbers, data from two facilities and two model sizes are available for comparison, whereas at Mach 5 and 8 results from several sources are compared. The Reynolds numbers were selected as close as possible to being the same at each nominal Mach number; thus, the differences shown should be attributable, for the most part, to precision of measurement factors. With the exception of C_m at Mach 2 (Fig. 3a), the curves have been faired with due consideration given all sources to establish a correlation of the data. Although a significant discrepancy in C_m at $M_\infty = 2$ exists for the 4.0-in. model, a thorough examination of all possible causes failed to reveal a satisfactory reason. As will be documented later in Figs. 6 and 7, these curves may be considered applicable for a fairly broad Reynolds number range.

The static stability characteristics of HB-2 are documented in Figs. 4 and 5. More data are available for comparison because of the

extensive tests reported by the ONERA for the HB-2 model. As a matter of interest and additional verification, values derived from integration of longitudinal-circumferential pressure distributions (Ref. 9) are included for a nominal 10-deg angle of attack. In general, it appears that excellent agreement exists between the force data. The most significant differences are apparent for the pitching-moment coefficient in the hypersonic range, $M_\infty \geq 6$. However at Mach 8, for example, the variations in C_m for $\alpha \approx 12$ deg (see Fig. 5b) amount to less than a ± 3-percent variation in center of pressure.

Inasmuch as the forebody axial force is not greatly influenced by angle-of-attack variation, a comparison of angle-of-attack data is considered unnecessary. However, typical Mach number effects on C_A versus α may be found in Ref. 1. It is shown that C_A decreases slightly with α for $M_\infty < 3$, whereas it increases with angle of attack at Mach numbers above 3.

The influence of Reynolds number on the parameters C_{N_α}, x_{cp}/ℓ, C_A, and C_{A_b} are shown in Figs. 6 through 9 for model HB-1 and in Figs. 10 through 13 for model HB-2. With regard to the influence on test data for model HB-1, it may be said, in general, that the Reynolds number effect is quite small. At Mach 20, however, the forebody drag (Fig. 8b) is especially sensitive to Reynolds number variations because of the large friction contribution associated with the very low local Reynolds numbers. Fewer data are shown for base drag in Fig. 9a, since those data are excluded for which the sting did not approach the specification. The base drag coefficient appears to be rather insensitive to Reynolds number, when considering the trends for Mach 8 and 10.

Conversely, model HB-2 aerodynamic characteristics are shown in Figs. 10, 11, and 12 to be significantly dependent upon the Reynolds number. At supersonic speeds ($M_\infty \leq 5$), these effects are caused by the occurrence of laminar boundary-layer separation induced by the interaction of the boundary layer with the adverse pressure gradient at the flare. Pitching perturbations produce circumferential variations in the extent of separation, thus causing abnormal differential pressure loadings, particularly in the region near reattachment. Since the relative extent of this separation is an inverse function of the Reynolds number (Ref. 10), the variations are to be expected. At hypersonic speeds, flow separations tend to disappear, but when they do exist the longitudinal pressure gradients are significantly less than those found at intermediate supersonic speeds. Thus, the rapid changes in pressure between the windward and leeward sides of the flare do not occur. As a consequence, Reynolds number has a small effect on the initial normal-force curve slope above Mach 5 (see Fig. 10b). The initial center-of-pressure location is affected

in a similar manner, of course, as is evident in Fig. 11. From these data in Figs. 10 and 11, it may be observed that the agreement among the various data sources is excellent; hence, the fairings are judged to be suitable reference correlation curves.

The forebody axial-force coefficient of model HB-2 at zero lift is given in Fig. 12 as a function of Reynolds number, Re_d, for the Mach number range, 1.5 to 20. Wave drag coefficients (pressure integrations) at maximum Reynolds number, primarily from Ref. 9, are included and show, as expected, that the friction drag is nearly insignificant at these Reynolds numbers up to Mach 8. An interesting difference in the influence of Reynolds number is shown by the data at Mach numbers greater than and less than Mach 5. At low supersonic speeds, for example Mach 3, decreasing Reynolds number is in the direction for increasing extent of flow separation. Flow separation as well as thickened boundary layers decrease the initial pressure rise on conical frustums; thus, the forebody axial-force coefficient would be expected to decrease with a reduction in Reynolds number because the drag contribution of the flare is correspondingly reduced. However, at hypersonic speeds the flare pressure distribution is basically unaffected by comparable Reynolds number variations (see Fig. 17). Hence, the wave drag remains nearly fixed, and the low local Reynolds number, which is caused by the increased bow-wave total pressure losses, now produces a relatively large skin friction contribution which is the reason for an increasing drag coefficient as Reynolds number is reduced. That this effect becomes quite appreciable is especially clear at $M_\infty \geq 16$, which is shown in Fig. 12b. These data as well as the data for HB-1 from Fig. 8b are replotted in Fig. 13 in terms of the viscous interaction parameter, $\overline{V}_\infty$. It should be noted that for infinite Reynolds number (when $\overline{V}_\infty$ equals zero) these data extrapolate to the value indicated for the wave drag only.

The base axial-force coefficient variation (for α = 0 deg) with Reynolds number is indicated in Fig. 14 for model HB-2. Since the data at each Mach number are fairly limited, a true correlation is not possible. However, the data at Mach 5 and 8 indicate that excellent correlation is to be anticipated.

The effect of Mach number on the parameters discussed is shown in Fig. 15 for both model HB-1 and model HB-2 at the condition of maximum Reynolds number as indicated by the double abscissa. For reference, the magnitude of these parameters as predicted by the modified Newtonian theory at Mach 10 is indicated. Only the drag is closely estimated. The declining base drag contribution at high Mach numbers is particularly evident in Fig. 15c; however, the trend at Mach 10 suggests that the assumption of zero base drag for Mach 20 may not entirely be justified.

It should be noted that these base drag data were obtained by measuring the cavity pressure inside the model.

Dynamic stability data for model HB-2 are shown in Fig. 16 in terms of the damping-in-pitch derivatives versus Reynolds number at Mach 2, 3, and 4. These data were obtained by Ward of the VKF using a small-amplitude, forced-oscillation, balance system which incorporates a cross flexure for pitch oscillations only. The data were obtained at the natural frequency of the model-balance system and were corrected for model damping in still air. Although no other results are available, these data show the usual decrease of damping-in-pitch with Mach number increase and a pronounced dependence on Reynolds number at Mach 4.

3.2 PRESSURE AND HEAT-TRANSFER MEASUREMENTS

Selected longitudinal pressure distribution results for zero-degree angle of attack are presented in Fig. 17 for Mach numbers from 1.5 to 18 at high and low Reynolds numbers. Although more detailed results may be found in Ref. 9, these data show the variation of the Reynolds number influence with Mach number for model HB-2. Since the flare angle is small, only laminar flow separations are possible (Ref. 10). The first indication of separation is to be noted at Mach 2 by the slight pressure increase near the beginning of the flare ($x/\ell \approx 0.6$). This is the plateau pressure rise caused by the stable reverse flow region ahead of the flare. This pressure rise clearly increases at Mach 3 and 4 for the low Reynolds number condition. Since there is no flow separation at the maximum Reynolds number, the boundary layer obviously was turbulent. At Mach 5, flow separation was present even at the maximum Reynolds number, since boundary-layer transition was delayed sufficiently by the Mach number increase. However, data at Mach 8 and 18 demonstrate quite clearly the elimination of laminar flow separation through the influence exerted by the appreciable Mach number increase. Thus, as noted already in Figs. 10 and 11, significant Reynolds number effects caused by flow separation are to be expected only in the supersonic speed range.

Data obtained at only Mach 8 and 20 are currently available for model HB-1, and these are given in Fig. 18. They are also included in Fig. 17 to illustrate better the flare pressure rise. A comparison of available pressure data is made in Fig. 19. The differences are negligible at Mach 2 and 3, whereas they become increasingly pronounced with Mach number. This situation exists simply because of the resolution capabilities of the transducer system employed. At Mach 8, however, a higher resolution transducer was used for stations at $x/\ell = 0.16$, 0.30, and 0.45, and the agreement is markedly improved. The agreement,

however, is much better between the ONERA Mach 16.5 data and VKF data at Mach 18 because the transducers used were chosen specifically for one pressure range.

The only reliable heat-transfer data presently available are those at zero lift, for about Mach 18, shown in Fig. 20. Results for both models are presented in terms of the heat transfer relative to the stagnation level versus the nondimensional surface distance. The heat-transfer rates, which were measured with calorimeter-type gages, for both models are in excellent agreement.

Longitudinal pressure distributions at three circumferential positions are given in Fig. 21, at an angle of attack of approximately 10 deg, for model HB-2. The corresponding distributions of local normal-force coefficient and local axial-force coefficient are shown in Fig. 22. It may be observed that at Mach 3 or greater the load distributions are qualitatively the same.

4.0 CONCLUSIONS

All of the available experimental results on the standard ballistic models HB-1 and HB-2 have been examined in some detail to establish correlation curves which document the aerodynamic performance of these configurations. A few general observations, to highlight the most noteworthy characteristics of these models, follow:

1. Although the aerodynamic parameters for model HB-1 are only slightly affected by Reynolds number, the greatest effect is observed on drag at Mach 20. Mach number variations change the stability parameters to an appreciable extent for $M_\infty \leq 5$, whereas the zero-lift forebody axial-force coefficient is relatively invariant for $M_\infty \leq 10$.

2. Because of laminar boundary-layer separation, all aerodynamic (stability and drag) parameters for model HB-2 in the supersonic range ($2 \leq M_\infty \leq 5$) are sensitive to Reynolds number variations; however, the data are satisfactorily correlated by the Reynolds number, Re_d, at all Mach numbers regardless of model size. At high Mach numbers ($M_\infty > 8$) the zero-lift axial-force coefficient becomes sensitive to Reynolds number variation because of viscous effects.

3. In general, excellent correlation was found among the test data from various facilities in the United States and France, and from from one facility in England.

REFERENCES

1. Hills, R. "A Review of Measurements on AGARD Calibration Models." AGARDograph 64, November 1961.

2. Gray, J. Don and Lindsay, E. Earl. "Force Tests of Standard Hypervelocity Ballistic Models HB-1 and HB-2 at Mach 1.5 to 10." AEDC-TDR-63-137, August 1963.

3. Private Communication from P. Carriere, ONERA, to J. Lukasiewicz, AEDC-VKF, January 1964.

4. Cable, A. J. and Bowman, J. E. "Hypersonic Wind Tunnel Measurements of the Normal Forces and Centres of Pressure of Three Cone-Cylinder-Flare Models." RARDE Memorandum (B) 1962.

5. Deem, R. E. "Pressure and Heat-Transfer Distribution Tests on a Standard Ballistic-Type Model HB-2 at Mach 2 to 5, Including the Effects of Shock Impingement." Douglas Aircraft Co, Inc., Report S-R6, June 1961.

6. Test Facilities Handbook (5th Edition). "von Kármán Gas Dynamics Facility, Vol. 4." Arnold Engineering Development Center, July 1963.

7. Maydew, R. C. "Sandia Laboratory Aerodynamic Test Facilities." SC-4937(M), September 1963.

8. Rebuffet, P. "Les Souffleries Hypersoniques de Recherches de l'O. N. E. R. A." Jahrbuch der W. G. L., 1960.

9. Jones, J. H. "Pressure Tests on the Standard Hypervelocity Ballistic Model HB-2 at Mach 1.5 to 5." AEDC-TDR-64-, to be published.

10. Gray, J. Don. "A Correlation of Axisymmetric Laminar Flow Separation Characteristics." Paper presented in AIAA 1st Annual Meeting in Washington, D. C., June 29 - July 2, 1964.

TABLE 1

SUMMARY OF EXPERIMENTAL RESULTS

Facility	Facility Ref.	Data Ref.	Model Config.	d, in.	Sting D/d	Sting L/d	β, deg	Nominal Mach Number	$Re_d \times 10^{-6}$	α, deg	Tests* F	Tests* P	Tests* H	Remarks
AEDC, VKF, 40 in. x 40 in. Supersonic Tunnel (A)	6	2	HB-1 & -2	4.00	≤ 0.3	≥ 3.0	20	1.5, 2, 3, 4, & 5	0.35 to 2.53	-1 to 14	x			
AEDC, VKF, 40 in. x 40 in. Supersonic Tunnel (A)	6	Unpub.	HB-2	4.00	-	-	-	2, 3, 4	0.40 to 2.00	0	x			Dynamic Stability Data
AEDC, VKF, 40 in. x 40 in. Supersonic Tunnel (A)	6	2	HB-1 & -2	1.25	0.6 & 0.8	6.4	-	1.5, 2, 3, 4, & 5	0.11 to 0.78	-1 to 14	x			
AEDC, VKF, 12 in. x 12 in. Supersonic Tunnel (D)	6	2	HB-1 & -2	1.25	0.6 & 0.8	6.4	-	1.5, 2, 3, 4, & 5	0.04 to 1.68	-1 to 14	x			
AEDC, VKF, 50 in. Mach 8 Tunnel (B)	6	2	HB-1 & -2	7.50	0.3	3.0	20	8	0.55 to 2.18	-2 to 14	x			
AEDC, VKF, 50 in. Mach 8 Tunnel (B)	6	2	HB-1 & -2	4.00	0.3	3.0	20	8	0.29 to 1.12	-2 to 14	x			
AEDC, VKF, 50 in. Mach 10 Tunnel (C)	6	2	HB-1 & -2	7.50	0.3	3.0	20	10	0.19 to 1.36	-2 to 14	x			
AEDC, VKF, 12 in. x 12 in. Hypersonic Tunnel (E)	6	Unpub.	HB-1 & -2	2.50	0.3	3.0	20	5, 6, 7, & 8	0.60 to 2.65	-2 to 12	x			
AEDC, VKF, 50 in. Hypervelocity Tunnel (H)	6	Unpub.	HB-1 & -2	2.00	~0.5	~6.0	-	18 - 21	0.01 to 0.09	0	x			Axial-Force Measurements Only
Sandia Corporation, 18-in.-diam, Hypersonic	7	Unpub.	HB-1 & -2	2.00	0.38	2.7	5	5.3 & 7.5	0.10 to 0.20	-2 to 20	x			
RARDE, No. 3 Hypersonic Gun Tunnel	4	4	HB-2	1.00	≤ 0.5	≤ 4.0	-	8.4 & 10.3	0.14 & 0.30	+3 to 21	x			No Axial-Force Measurements
ONERA S5 Chalais, 0.3 m x 0.3 m	3	3	HB-2	1.18	0.5	2.0	14	1.6, 2.2, 3.1	0.16 to 0.23	-5 to 8	x			With Boundary-Layer Trips Also
LBRA C4 Vernon, 0.4 m x 0.4 m	3	3	HB-2	1.18	0.5	1.5	5	2.1, 3.2, 4.3	0.41 & 0.82	-4 to 8	x			
ONERA SR2 Chalais, 0.3-m Diam	8	3	HB-2	1.18	0.5	1.9	9	6, 7	0.82	-5 to 10	x			Preliminary Data
ONERA SR'3 Chalais, 0.12-m Diam	8	3	HB-2	1.18	0.5	4.2	7.2	10	0.20	-5 to 10	x			
ONERA ARC 1 Fontenay, 0.5-m Diam	8	3	HB-2	2.35	0.4	5.3	-	16.5	0.16	-1 to 10	x			
AEDC, VKF, 40 in. x 40 in. Supersonic Tunnel (A)	6	9	HB-2	4.00	≤ 0.3	≥ 3.0		1.5, 2, 3, 4, & 5	0.33 to 2.81	-3 to 15		x		At M_∞ = 2 & 4, α = 0 only
AEDC, VKF, 50 in. Mach 8 Tunnel (B)	6	Unpub.	HB-1	7.50	0.3	3.0		8	0.62 to 2.13	-15 to 15		x		
AEDC, VKF, 50 in. Mach 8 Tunnel (B)	6	Unpub.	HB-1 & -2	4.00	0.3	3.0		8	0.18 to 1.07	-15 to 15		x		
AEDC, VKF, 50 in. Hypervelocity Tunnel (H)	6	Unpub.	HB-1 & -2	4.00	~0.5	~6.0		17.6 to 20	0.03 to 0.12	0		x	x	
Douglas Aerophysics Laboratory Supersonic 4-ft Tunnel	5	5	HB-2	3.75	0.53	3.0		2, 3, 4, & 5	3.8 to 7.1	0 & 20		x		
ONERA Arc 1 Fontenay, 0.5-m Diam	3	3	HB-2	2.35	-	-		16.5	0.16	0 & 5		x		Preliminary Data
David Taylor Model Basin, 13.5-in. Hypersonic Tunnel	-	Unpub.	HB-1 & -2	2.75	0.3	-		7	0.10 to 0.63	0		x		Unresolved Discrepancies

*Types of Tests: F - Static Force (except as noted)
 P - Pressure Distribution
 H - Heat-Transfer Distribution

9
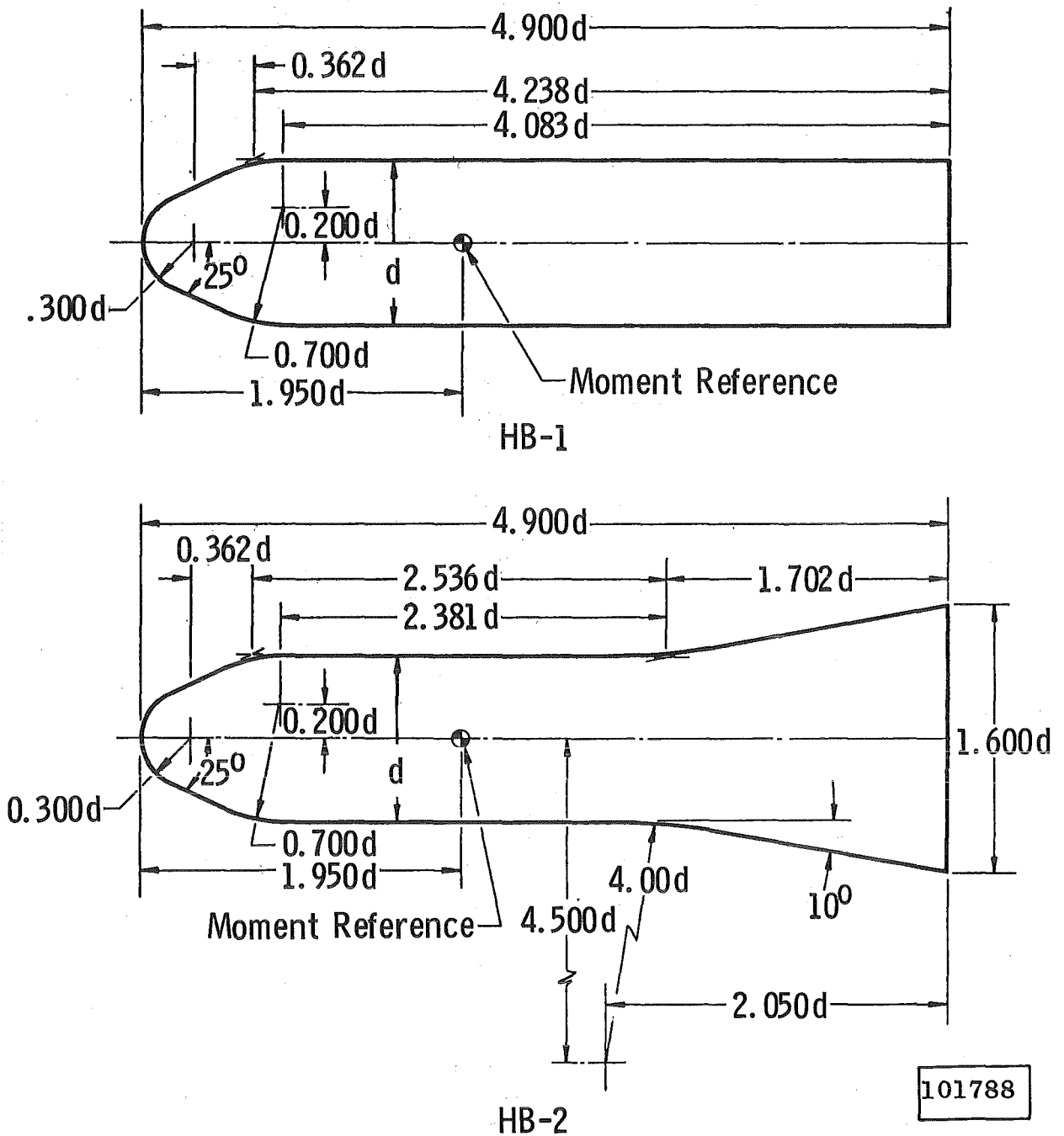
a. Models HB-1 and HB-2

Fig. 1 Standard Model and Sting Configurations

L = 3.0 d

d

D = 0.3 d

β = 20 deg
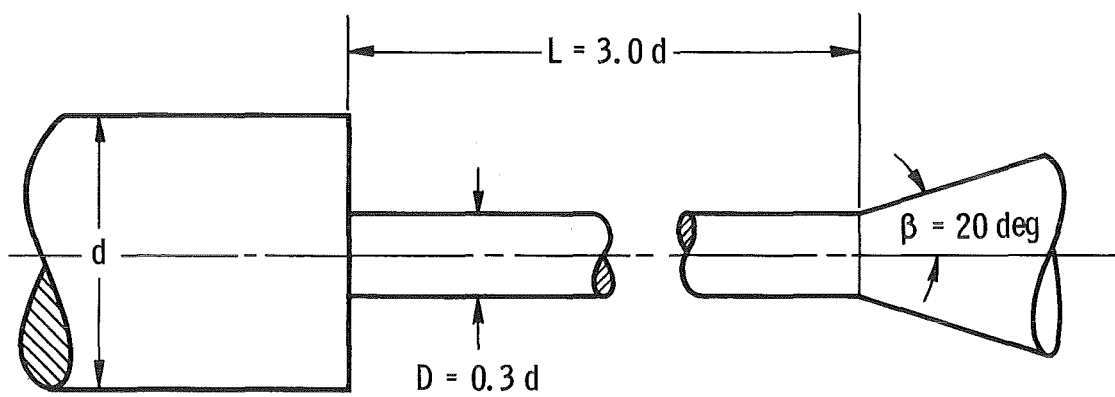
101789

b. Sting Geometry

Fig. 1 Concluded

Sym	M_∞	$Re_d \times 10^{-6}$	d, in.	Facility
○	1.49	0.51	4.00	VKF (A)
●	1.50	0.43	1.25	VKF (A)
△	1.45	0.32	1.25	VKF (D)
○	2.00	0.86	4.00	VKF (A)
●	2.00	0.54	1.25	VKF (A)
△	2.00	0.82	1.25	VKF (D)
○	3.00	1.23	4.00	VKF (A)
●	3.01	0.78	1.25	VKF (A)
△	2.99	1.00	1.25	VKF (D)
○	4.01	0.55	4.00	VKF (A)
●	4.03	0.62	1.25	VKF (A)
△	3.97	0.58	1.25	VKF (D)
○	5.05	0.44	4.00	VKF (A)
●	5.08	0.34	1.25	VKF (A)
△	5.02	0.35	1.25	VKF (D)
▽	4.98	0.88	2.50	VKF (E)
◁	5.30	0.20	2.00	Sandia
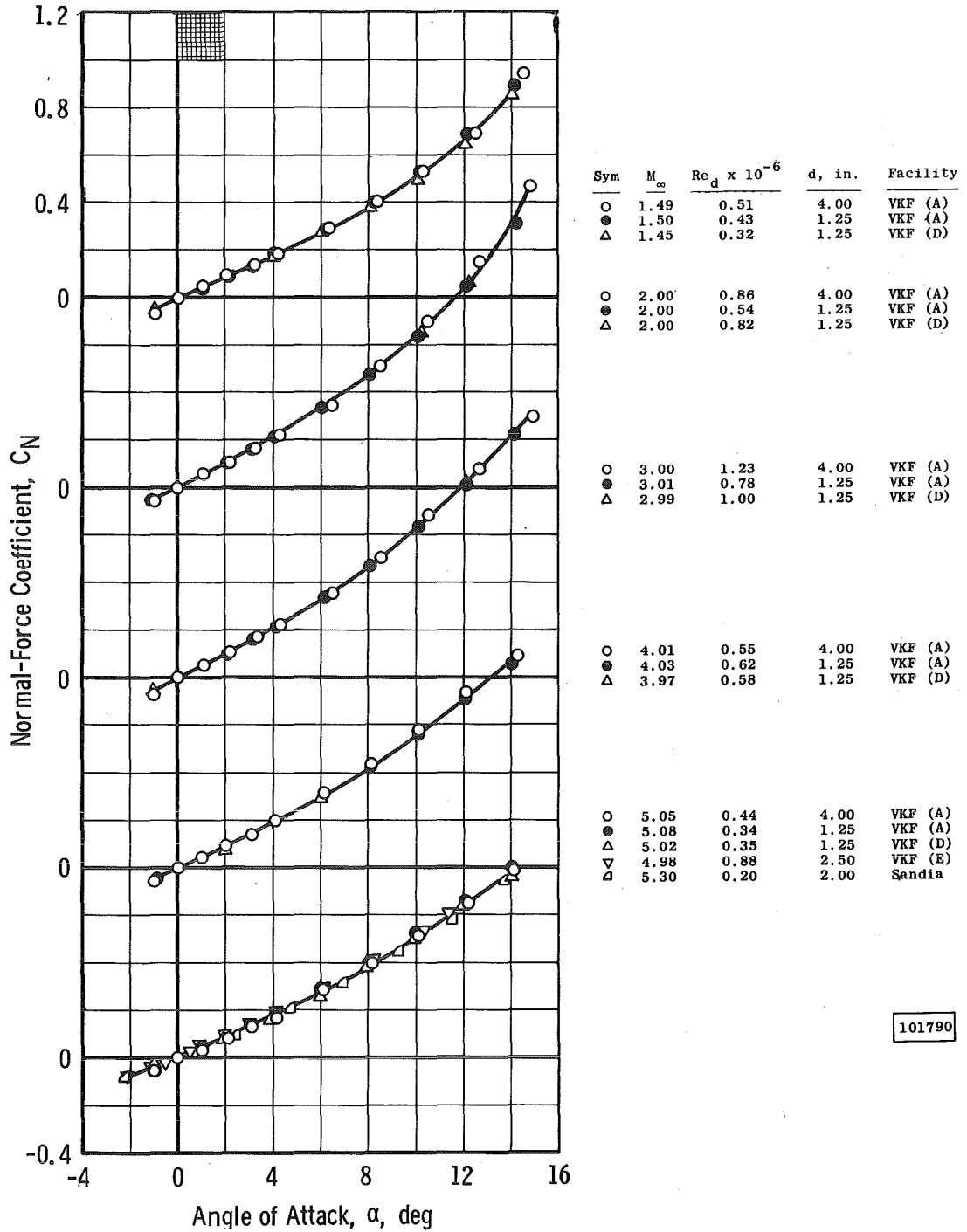
101790

a. Mach Numbers 1.5. 2, 3, 4, and 5

Fig. 2 Normal-Force Coefficient versus Angle of Attack for Model HB-1

13

b. Mach Numbers 6, 7, 8, and 10

Fig. 2 Concluded
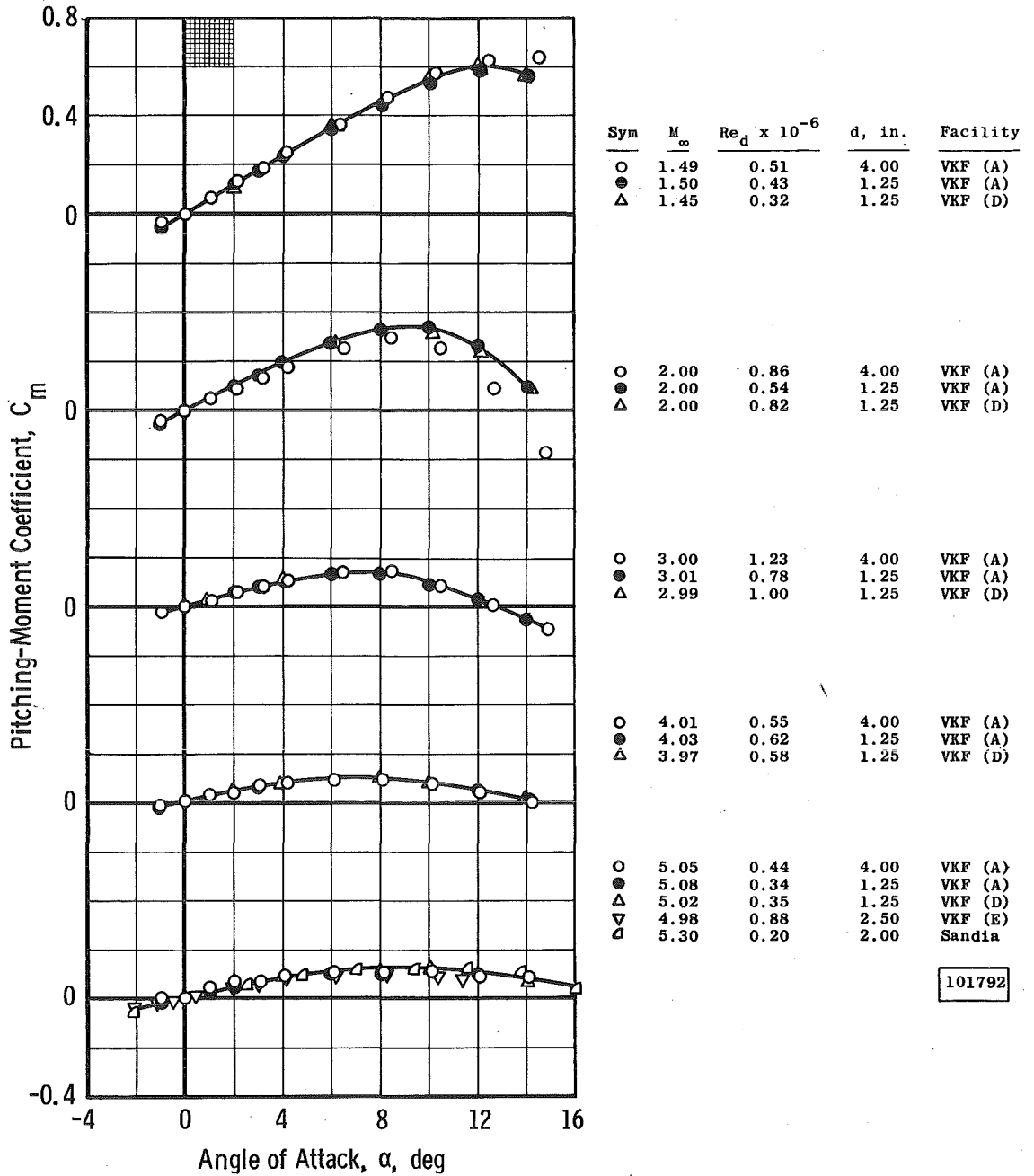
a. Mach Numbers 1.5, 2, 3, 4, and 5

Fig. 3 Pitching-Moment Coefficient versus Angle of Attack for Model HB-1

Sym	M_∞	$Re_d \times 10^{-6}$	d, in.	Facility
▽	6.04	0.98	2.50	VKF (E)
▽	7.13	1.00	2.50	VKF (E)
◻	8.07	1.05	7.50	VKF (B)
▣	8.09	1.12	4.00	VKF (B)
▽	8.02	1.06	2.50	VKF (E)
◿	7.50	0.17	2.00	Sandia
◇	10.18	1.36	7.50	VKF (C)
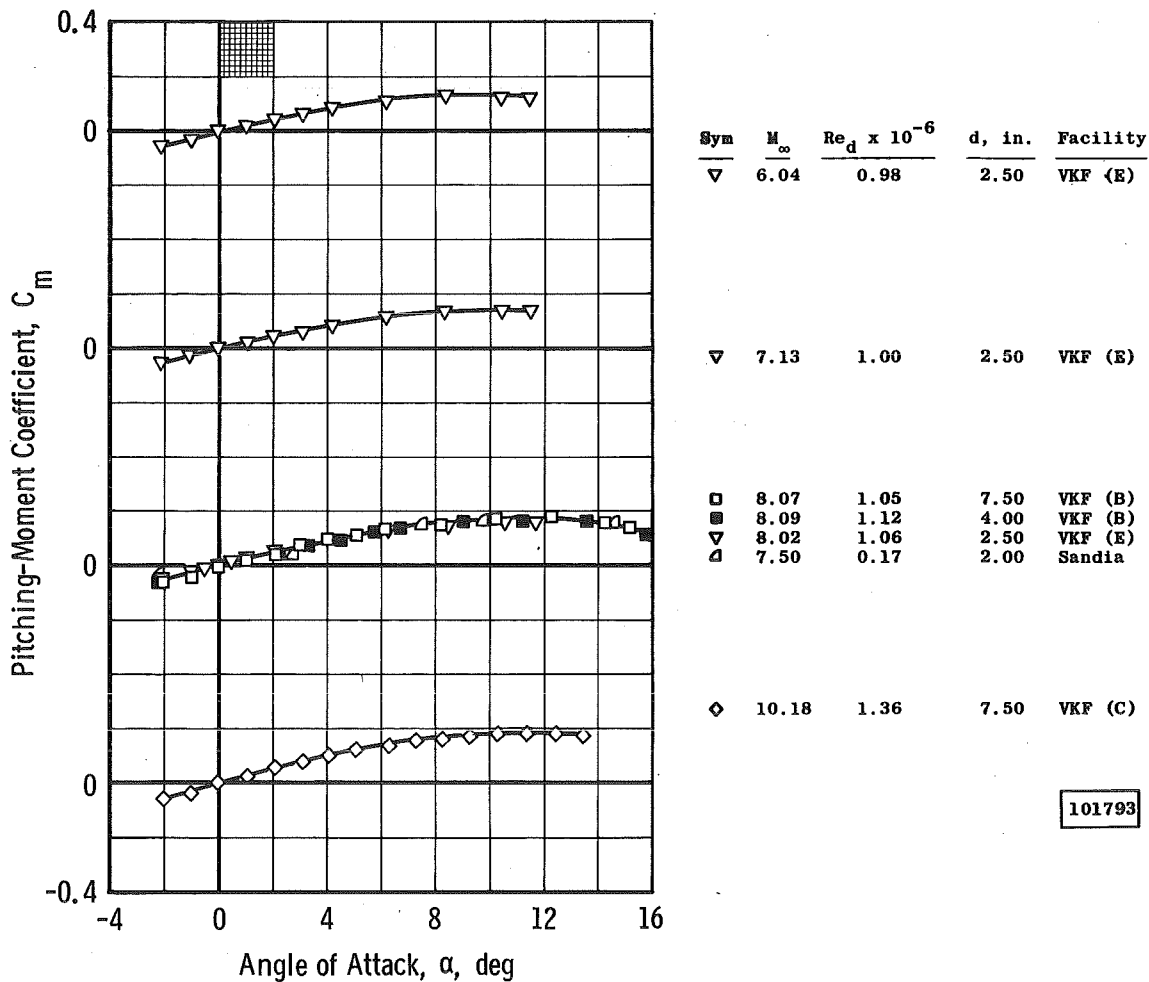
101793

b. Mach Numbers 6, 7, 8, and 10

Fig. 3 Concluded

Sym	M_∞	$Re_d \times 10^{-6}$	d, in.	Facility
O	1.50	0.99	4.00	VKF (A)
●	1.50	0.45	1.25	VKF (A)
△	1.45	0.69	1.25	VKF (D)
+	Pressure	Integration (See Fig. 22)		
O	1.99	0.82	4.00	VKF (A)
●	2.00	0.54	1.25	VKF (A)
△	2.00	0.52	1.25	VKF (D)
☆	2.12	0.41	1.18	LRBA (C4)
O	3.00	1.21	4.00	VKF (A)
◑	3.01	0.79	1.25	VKF (A)
△	2.99	1.01	1.25	VKF (D)
+	Pressure	Integration (See Fig. 22)		
☆	3.20	0.82	1.18	LRBA (C4)
O	4.01	0.60	4.00	VKF (A)
●	4.03	0.62	1.25	VKF (A)
△	3.97	0.61	1.25	VKF (D)
☆	4.26	0.82	1.18	LRBA (C4)
O	5.05	0.44	4.00	VKF (A)
●	5.08	0.34	1.25	VKF (A)
△	5.02	0.35	1.25	VKF (D)
▽	4.98	0.85	2.50	VKF (E)
◁	5.30	0.10	2.00	Sandia
+	Pressure	Integration (See Fig. 22)		

101794

a. Mach Numbers 1.5, 2, 3, 4, and 5

Fig. 4 Normal-Force Coefficient versus Angle of Attack for Model HB-2

Sym	M_∞	$Re_d \times 10^{-6}$	d, in.	Facility
▽	6.04	0.98	2.50	VKF (E)
☆	6.00	0.82	1.18	ONERA R2 Chalais
▽	7.13	1.00	2.50	VKF (E)
☆	7.00	0.82	1.18	ONERA R2 Chalais
□	8.07	1.07	7.50	VKF (B)
▨	8.09	1.12	4.00	VKF (B)
▽	8.02	1.07	2.50	VKF (E)
◿	7.50	0.17	2.00	Sandia
△	8.40	0.30	1.00	RARDE
+	Pressure Integration (See Fig. 22)			
◇	10.18	1.36	7.50	VKF (C)
◿	10.30	0.14	1.00	RARDE
△	10.00	0.20	1.18	ONERA R3 Chalais
◯	16.5	0.16	1.18	ONERA ARC 1 Fontenay

101795

b. Mach Numbers 6, 7, 8, 10 and 16.5

Fig. 4 Concluded

18

0.4

0

0

Pitching-Moment Coefficient, C_m

0

0

0

-0.4

-0.8

-1.2

-4   0   4   8   12   16

Angle of Attack, α, deg

Sym	M_∞	$Re_d \times 10^{-6}$	d, in.	Facility
O	1.50	0.99	4.00	VKF (A)
●	1.50	0.45	1.25	VKF (A)
△	1.45	0.69	1.25	VKF (D)
+	Pressure	Integration	(See Fig. 22)	

O	1.99	0.82	4.00	VKF (A)
●	2.00	0.54	1.25	VKF (A)
△	2.00	0.52	1.25	VKF (D)
☆	2.12	0.41	1.18	LRBA (C4)

O	3.00	1.21	4.00	VKF (A)
●	3.01	0.79	1.25	VKF (A)
△	2.99	1.01	1.25	VKF (D)
+	Pressure	Integration	(See Fig. 22)	
☆	3.20	0.82	1.18	LRBA (C4)

O	4.01	0.60	4.00	VKF (A)
●	4.03	0.62	1.25	VKF (A)
△	3.97	0.61	1.25	VKF (D)
☆	4.26	0.82	1.18	LRBA (C4)

O	5.05	0.44	4.00	VKF (A)
●	5.08	0.34	1.25	VKF (A)
△	5.02	0.35	1.25	VKF (D)
▽	4.98	0.85	2.50	VKF (E)
◁	5.30	0.10	2.00	Sandia
+	Pressure	Integration	(See Fig. 22)	

101796

a. Mach Numbers 1.5, 2, 3, 4, and 5

Fig. 5 Pitching-Moment Coefficient versus Angle of Attack for Model HB-2
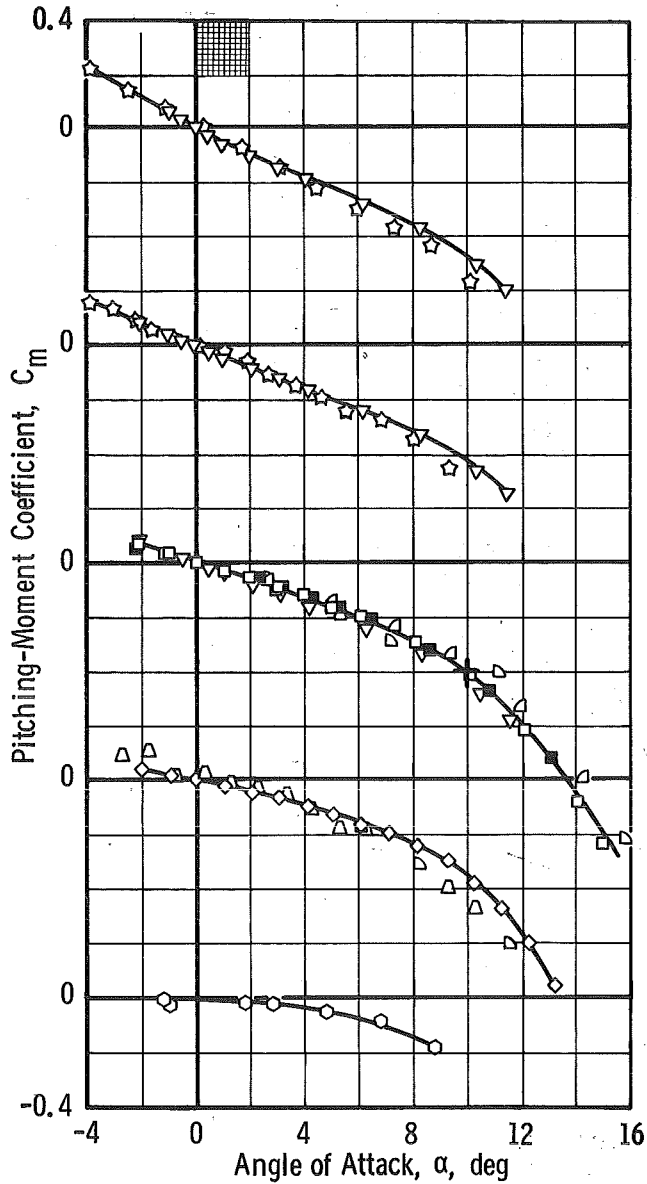
Sym	M_∞	Re_d x 10^{-6}	d, in.	Facility
▽	6.04	0.98	2.50	VKF (E)
☆	6.00	0.82	1.18	ONERA R2 Chalais
▽	7.13	1.00	2.50	VKF (E)
☆	7.00	0.82	1.18	ONERA R2 Chalais
□	8.07	1.07	7.50	VKF (B)
▣	8.09	1.12	4.00	VKF (B)
▽	8.02	1.07	2.50	VKF (E)
◢	7.5	0.17	2.00	Sandia
◿	8.4	0.30	1.00	RARDE
✛	Pressure Integration (See Fig. 22)			
◇	10.18	1.36	7.50	VKF (C)
◿	10.30	0.14	1.00	RARDE
△	10.00	0.20	1.18	ONERA R'3 Chalais
○	16.5	0.16	1.18	ONERA ARC 1 Fontenay

100952

b. Mach Numbers 6, 7, 8, 10, and 16.5

Fig. 5 Concluded
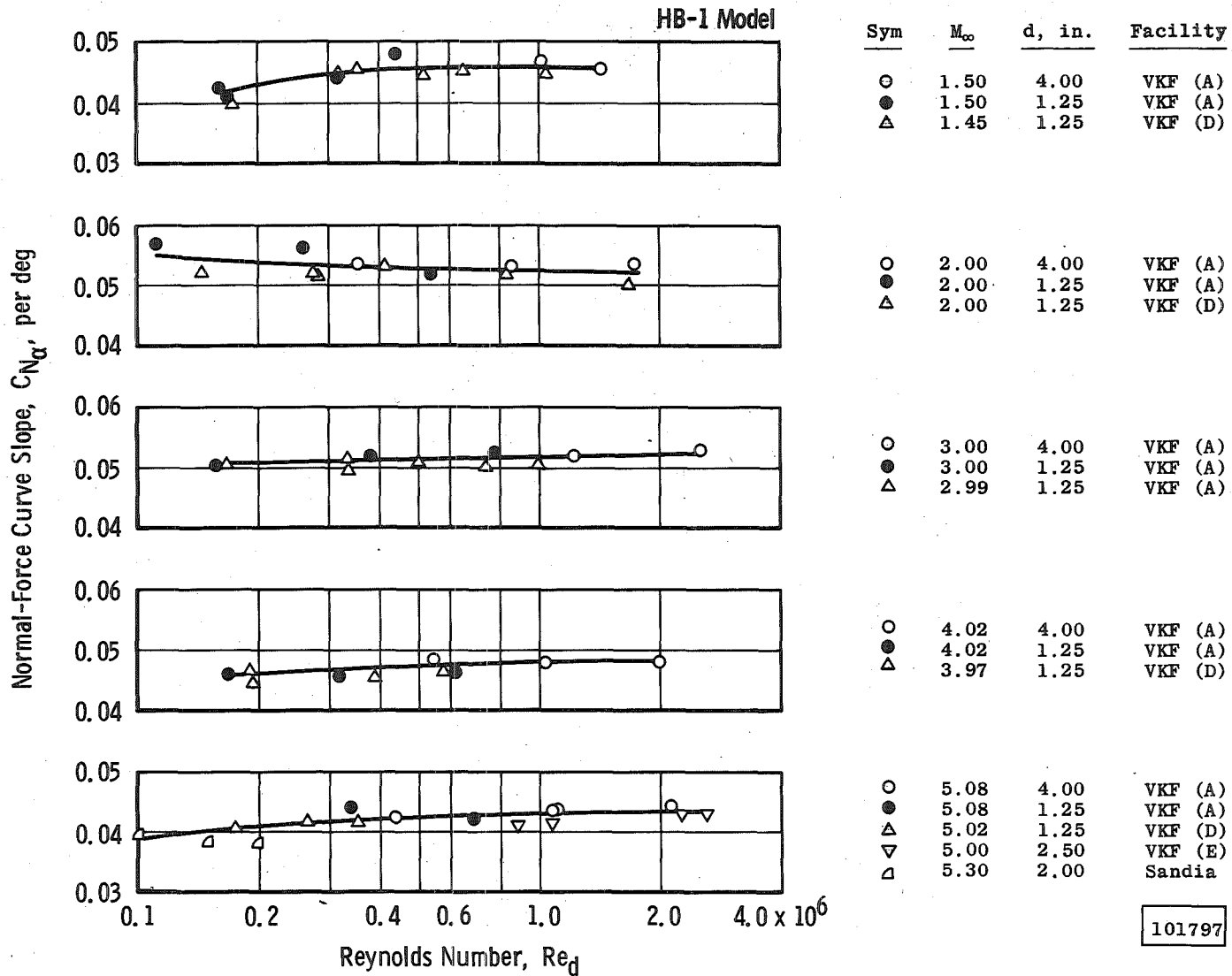
HB-1 Model

Normal-Force Curve Slope, C_{N_α}, per deg

0.05
0.04
0.03

0.06
0.05
0.04

0.06
0.05
0.04

0.06
0.05
0.04

0.05
0.04
0.03

Sym	M_∞	d, in.	Facility
⊙	1.50	4.00	VKF (A)
●	1.50	1.25	VKF (A)
△	1.45	1.25	VKF (D)
○	2.00	4.00	VKF (A)
●	2.00	1.25	VKF (A)
△	2.00	1.25	VKF (D)
○	3.00	4.00	VKF (A)
◐	3.00	1.25	VKF (A)
△	2.99	1.25	VKF (A)
○	4.02	4.00	VKF (A)
●	4.02	1.25	VKF (A)
△	3.97	1.25	VKF (D)
○	5.08	4.00	VKF (A)
●	5.08	1.25	VKF (A)
△	5.02	1.25	VKF (D)
▽	5.00	2.50	VKF (E)
◁	5.30	2.00	Sandia

101797

0.1   0.2   0.4   0.6   1.0   2.0   4.0 x 10⁶

Reynolds Number, Re_d

a. Mach Numbers 1.5, 2, 3, 4, and 5

Fig. 6 Initial Slope of Normal-Force Curve versus Reynolds Number for Model HB-1

AEDC-TDR-64-137

Normal-Force Curve Slope, CN_α, per deg

HB-1 Model
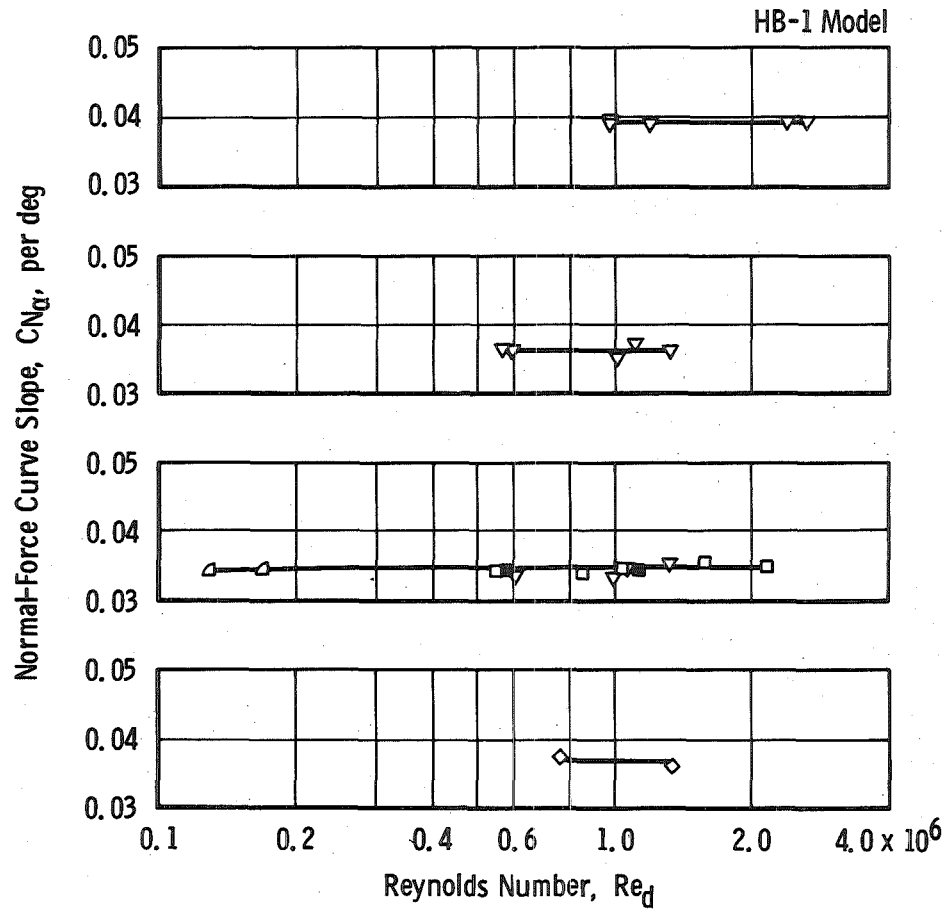
Sym	M_∞	d, in.	Facility
▽	6.06	2.50	VKF (E)
▽	7.07–7.20	2.50	VKF (E)
□	8.07	7.50	VKF (B)
▨	8.07	4.00	VKF (B)
▽	7.80–8.06	2.50	VKF (E)
◁	7.50	2.00	Sandia
◇	10.15	7.50	VKF (C)

101798

Reynolds Number, Re_d

b. Mach Numbers 6, 7, 8, and 10

Fig. 6 Concluded

HB-1 Model

Center-of-Pressure Location, x_{cp}/ℓ

Sym	M_∞	d, in.	Facility
⊖	1.50	4.00	VKF (A)
●	1.50	1.25	VKF (A)
△	1.45	1.25	VKF (D)

Sym	M_∞	d, in.	Facility
⊖	2.00	4.00	VKF (A)
●	2.00	1.25	VKF (A)
△	2.00	1.25	VKF (D)

Sym	M_∞	d, in.	Facility
○	3.00	4.00	VKF (A)
●	3.00	1.25	VKF (A)
△	2.99	1.25	VKF (D)

Sym	M_∞	d, in.	Facility
○	4.02	4.00	VKF (A)
●	4.02	1.25	VKF (A)
△	3.97	1.25	VKF (D)

Sym	M_∞	d, in.	Facility
○	5.08	4.00	VKF (A)
●	5.08	1.25	VKF (A)
△	5.02	1.25	VKF (D)
▽	5.00	2.50	VKF (E)
◁	5.30	2.00	Sandia

Reynolds Number, Re_d
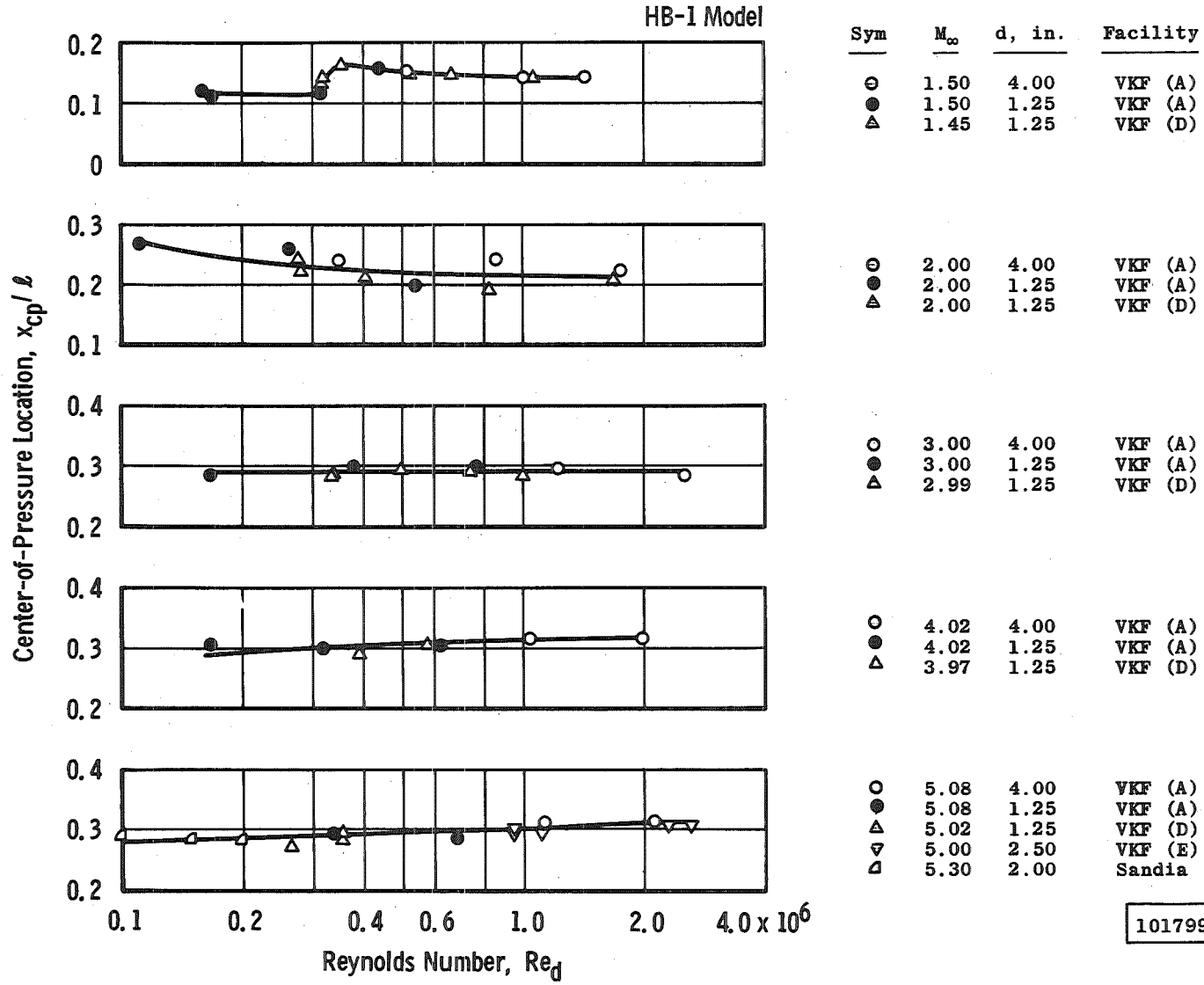
101799

a. Mach Numbers 1.5, 2, 3, 4, and 5

Fig. 7 Center of Pressure versus Reynolds Number for Model HB-1
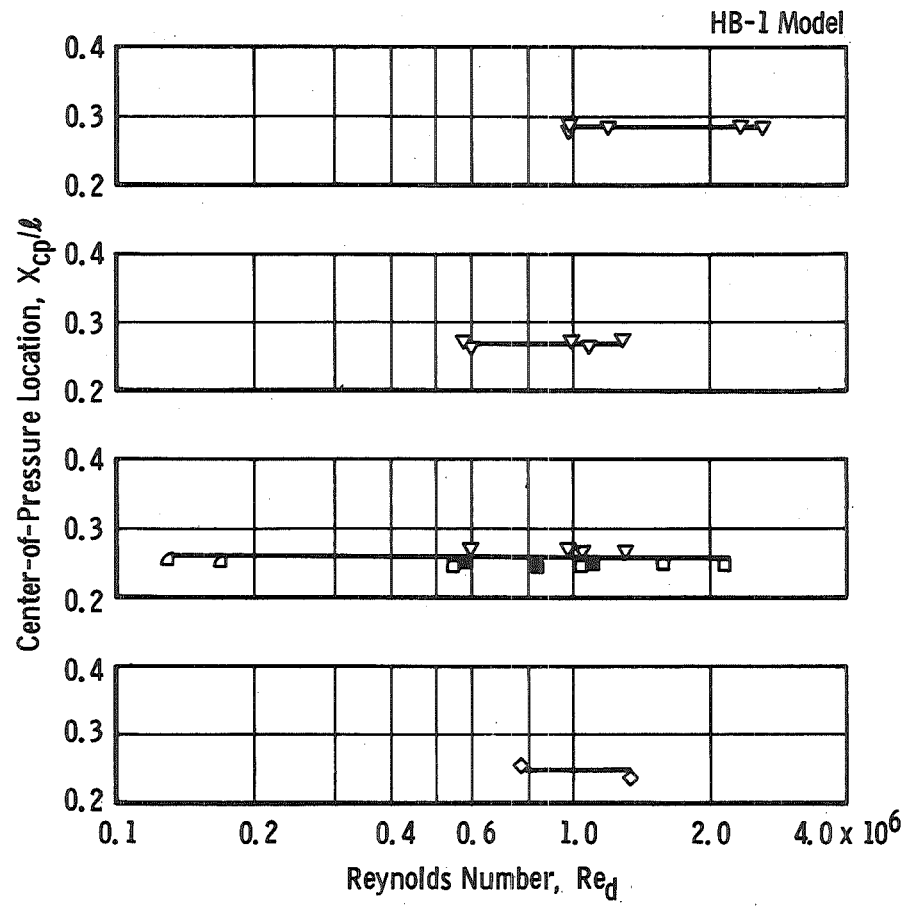
AEDC-TDR-64-137

b. Mach Numbers 6, 7, 8, and 10

Fig. 7 Concluded
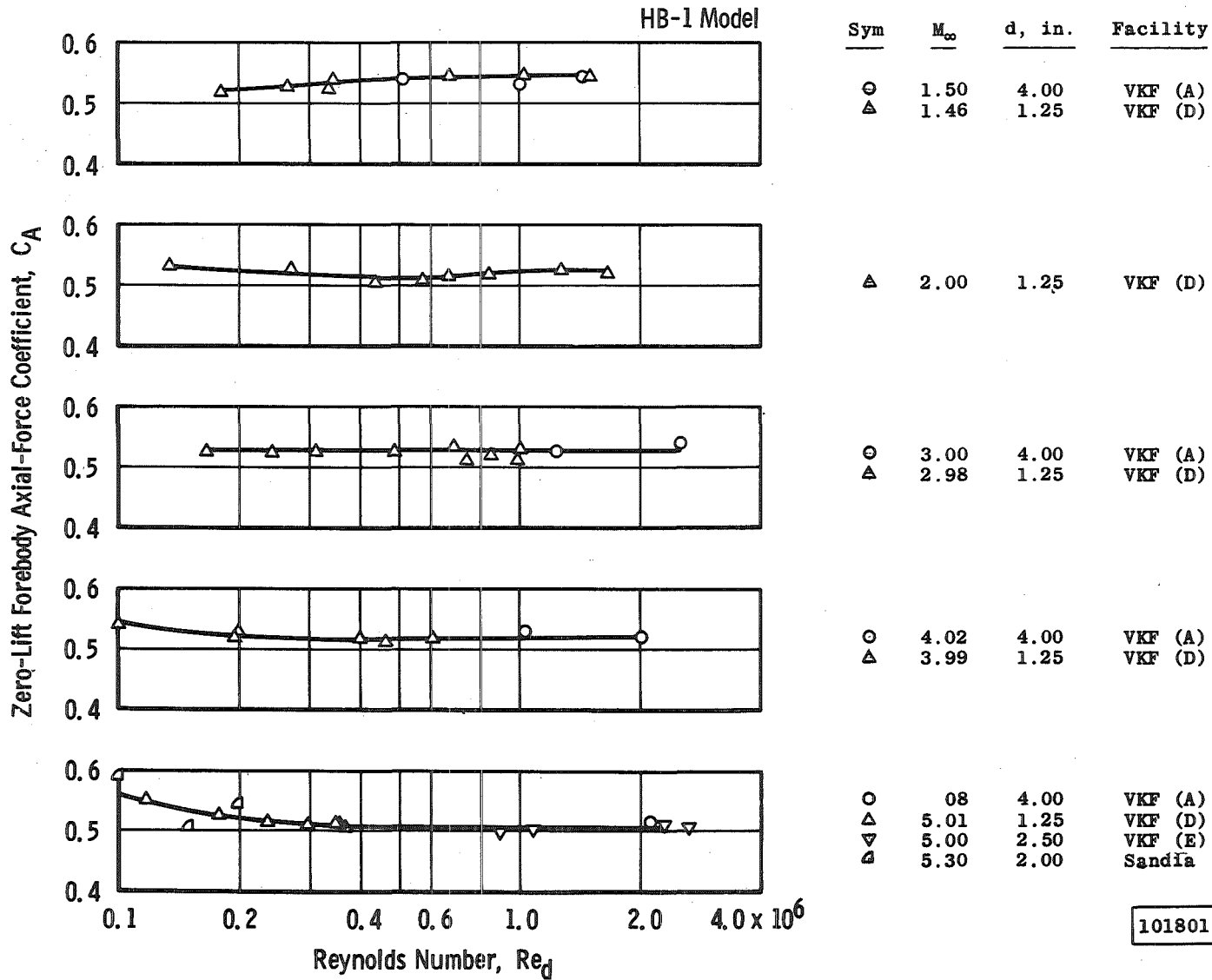
a. Mach Numbers 1.5, 2, 3, 4, and 5

Fig. 8 Zero-Lift Forebody Axial-Force Coefficient versus Reynolds Number for Model HB-1
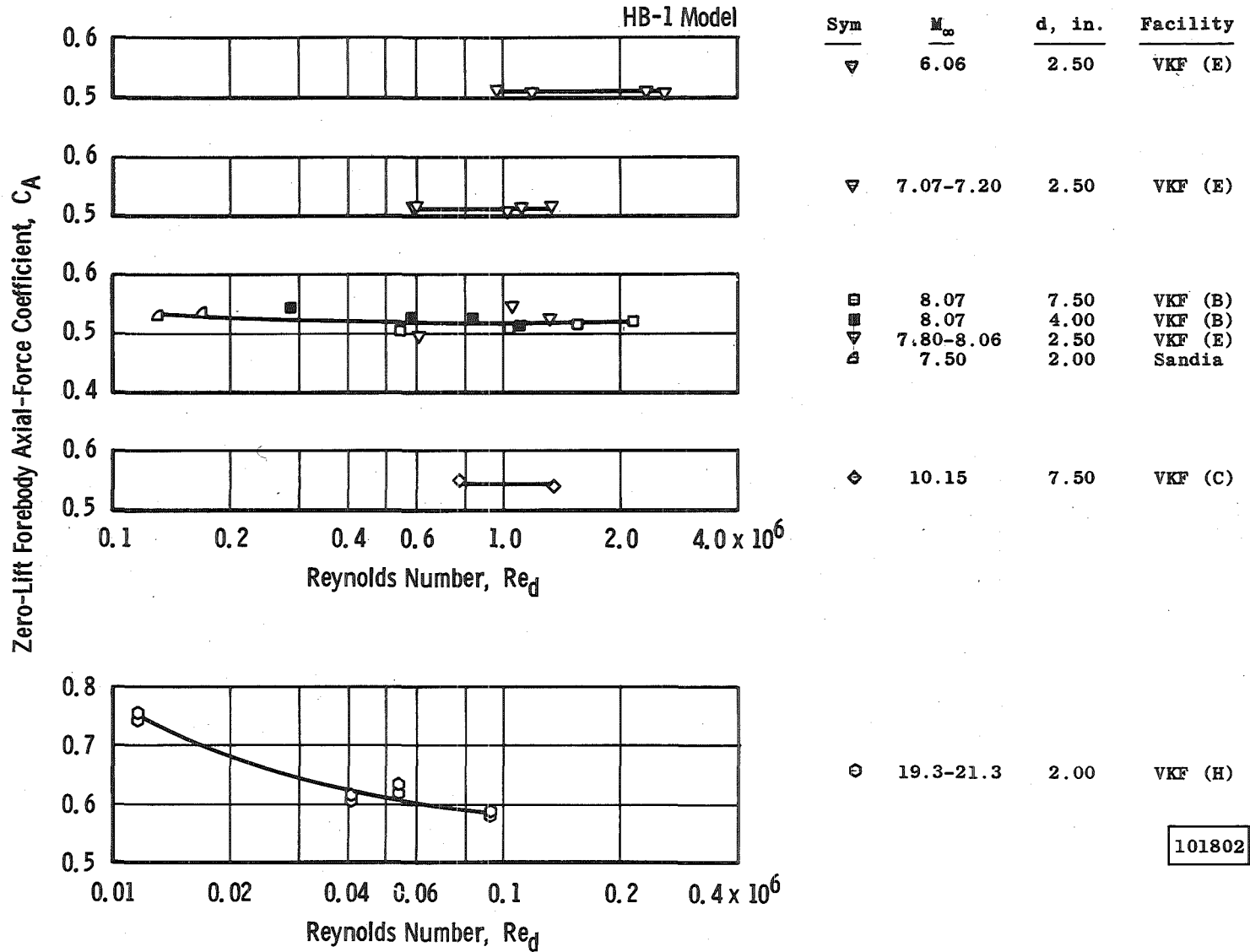
b. Mach Numbers 6, 7, 8, 10, and 20

Fig. 8 Concluded
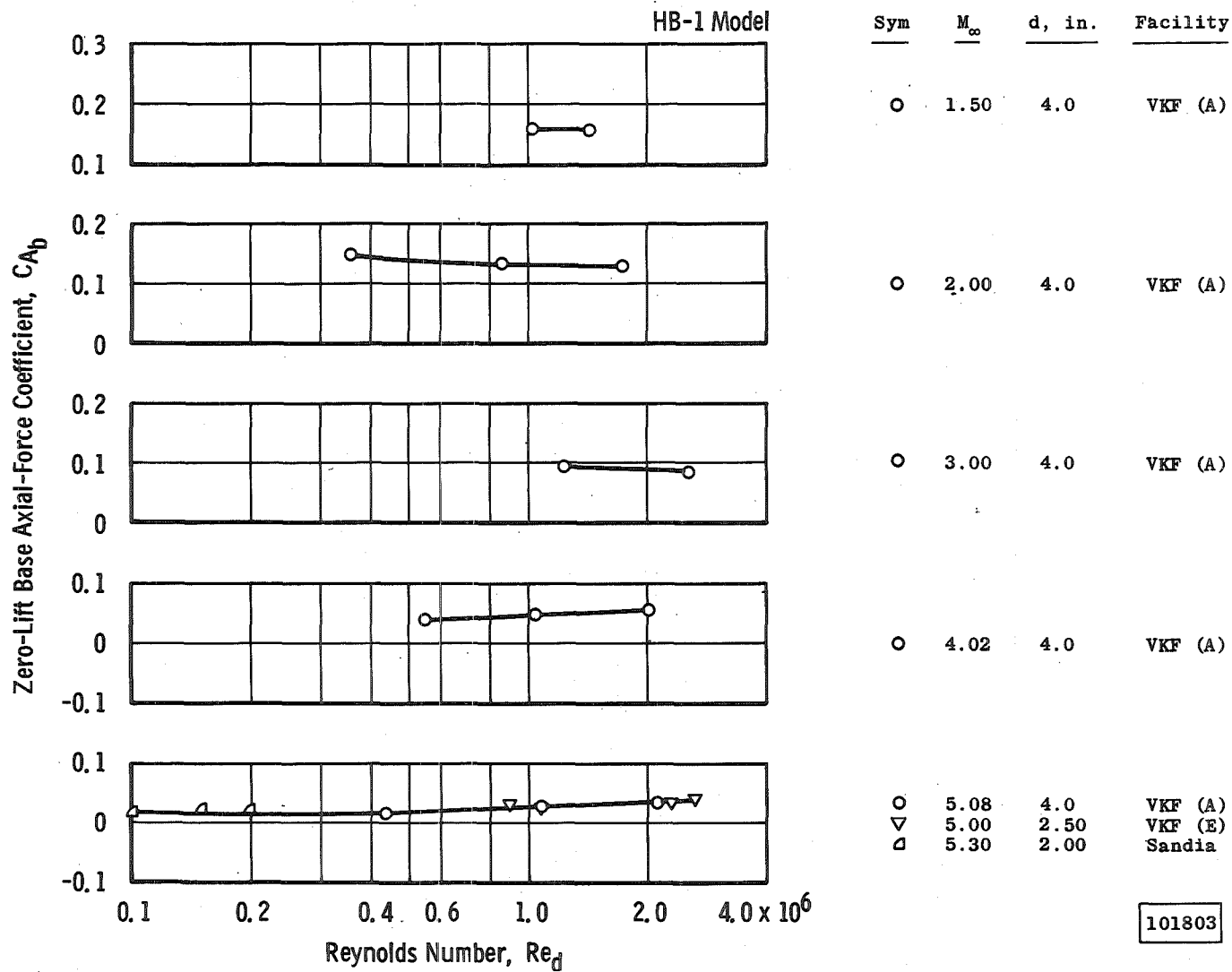
a. Mach Numbers 1.5, 2, 3, 4, and 5

Fig. 9 Zero-Lift Base Axial-Force Coefficient versus Reynolds Number for Model HB-1
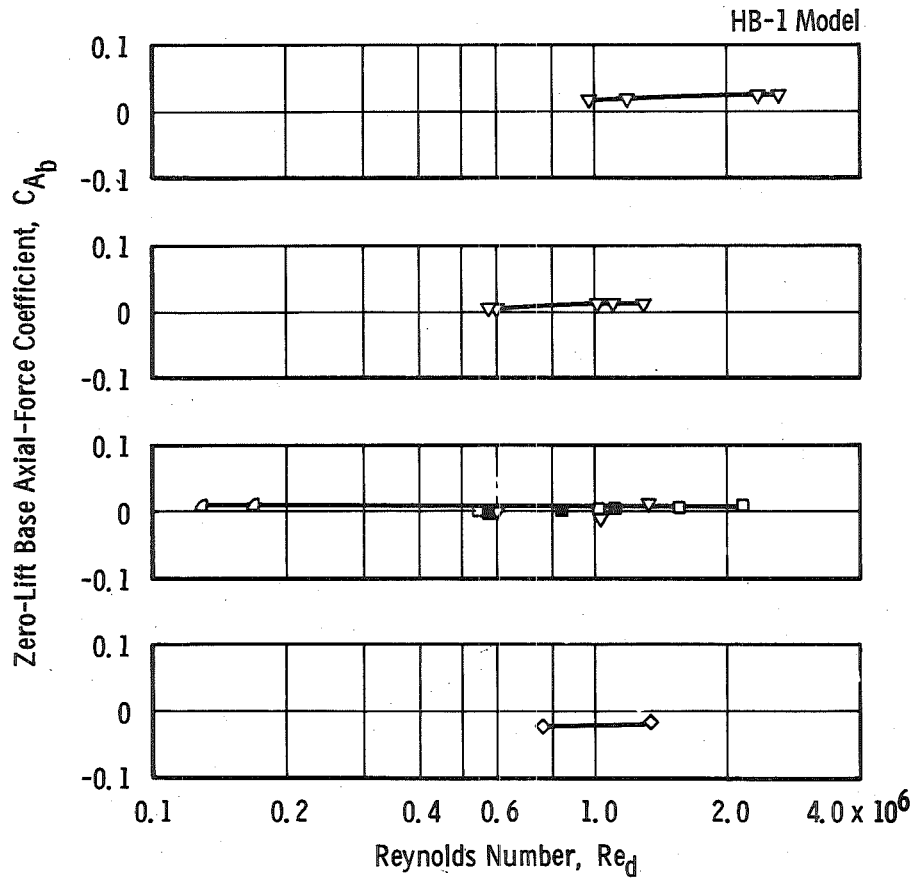
HB-1 Model

Sym	M_∞	d, in.	Facility
▽	6.06	2.50	VKF (E)
▽	7.07–7.20	2.50	VKF (E)
□	8.07	7.50	VKF (B)
▨	8.07	4.00	VKF (B)
▽	7.80–8.06	2.50	VKF (E)
◁	7.50	2.00	Sandia
◇	10.15	7.50	VKF (C)

Zero-Lift Base Axial-Force Coefficient, C_{A_b}

Reynolds Number, Re_d

101804

b. Mach Numbers 6, 7, 8, and 10

Fig. 9 Concluded

HB-2 Model

Normal-Force Curve Slope, C_{N_α}, per deg

0.09
0.08
0.07

0.10
0.09
0.08
0.07

0.11
0.10
0.09
0.08

0.10
0.09
0.08
0.07

Reynolds Number, Re_d

0.1   0.2   0.4   0.6   1.0   2.0 4.0×10^6

Sym	M_∞	d, in.	Facility
⊖	1.50	4.00	VKF (A)
●	1.50	1.25	VKF (A)
△	1.45	1.25	VKF (D)

○	2.00	4.00	VKF (A)
●	2.00	1.25	VKF (A)
△	2.00	1.25	VKF (D)
☆	2.12	1.18	LRBA (C4)

○	3.00	4.00	VKF (A)
●	3.00	1.25	VKF (A)
△	2.99	1.25	VKF (D)
☆	3.20	1.18	LRBA (C4)

○	4.02	4.00	VKF (A)
●	4.02	1.25	VKF (A)
△	3.97	1.25	VKF (D)
☆	4.26	1.18	LRBA (C4)

I01805

a. Mach Numbers 1.5, 2, 3, 4

Fig. 10 Initial Slope of Normal-Force Curve versus Reynolds Number for Model HB-2

HB-2 Model

Sym	M_∞	d, in.	Facility
○	5.08	4.00	VKF (A)
●	5.08	1.25	VKF (A)
△	5.01	1.25	VKF (D)
▽	5.00	2.50	VKF (E)
◿	5.30	2.00	Sandia
▽	6.06	2.50	VKF (E)
☆	6.00	1.18	ONERA R2 Chalais
▽	7.07-7.20	2.50	VKF (E)
☆	7.00	1.18	ONERA R2 Chalais
▢	8.07	7.50	VKF (B)
▨	8.07	4.00	VKF (B)
▽	7.80-8.06	2.50	VKF (E)
◿	7.50	2.00	Sandia
◿	8.40	1.00	RARDE
◇	10.15	7.50	VKF (C)
△	10.00	1.18	ONERA R'3 Chalais

101806

Normal-Force Curve Slope, C_{N_α}, per deg

Reynolds Number, Re_d

b. Mach Numbers, 5, 6, 7, 8, and 10

Fig. 10 Concluded

HB-2 Model

Center-of-Pressure Location, x_{cp}/ℓ

Reynolds Number, Re_d

0.6 — 0.5 — 0.4

0.6 — 0.5 — 0.4

0.7 — 0.6 — 0.5

0.7 — 0.6 — 0.5

0.7 — 0.6 — 0.5

0.1   0.2   0.4   0.6   1.0   2.0   4.0 x 10^6

Sym	M_∞	d, in.	Facility
○	1.50	4.00	VKF (A)
●	1.50	1.25	VKF (A)
△	1.45	1.25	VKF (D)
⊖	2.00	4.00	VKF (A)
●	2.00	1.25	VKF (A)
△	2.00	1.25	VKF (D)
☆	2.12	1.18	LRBA (C4)
○	3.00	4.00	VKF (A)
●	3.00	1.25	VKF (A)
△	2.99	1.25	VKF (D)
☆	3.20	1.18	LRBA (C4)
○	4.02	4.00	VKF (A)
●	4.02	1.25	VKF (A)
△	3.97	1.25	VKF (D)
☆	4.26	1.18	LRBA (C4)
○	5.08	4.00	VKF (A)
●	5.08	1.25	VKF (A)
△	5.01	1.25	VKF (D)
▽	5.00	2.50	VKF (E)
◁	5.30	2.00	Sandia

101807

a. Mach Numbers 1.5, 2, 3, 4, and 5

Fig. 11 Center of Pressure versus Reynolds Number for Model HB-2

HB-2 Model

Center-of-Pressure Location, x_{cp}/ℓ

0.6
0.5
0.4

0.6
0.5
0.4

0.6
0.5
0.4

0.6
0.5
0.4

0.1   0.2   0.4   0.6   1.0   2.0   4.0x10^6

Reynolds Number, Re_d

Sym	M_∞	d, in.	Facility
▽	6.06	2.50	VKF (E)
☆	6.00	1.18	ONERA R2 Chalais
▽	7.07-7.20	2.50	VKF (E)
☆	7.00	1.18	ONERA R2 Chalais
⊟	8.07	7.50	VKF (B)
▧	8.07	4.00	VKF (B)
▽	7.80-8.06	2.50	VKF (E)
△	7.50	2.00	Sandia
◇	10.15	7.50	VKF (C)
△	10.00	1.18	ONERA R'3 Chalais
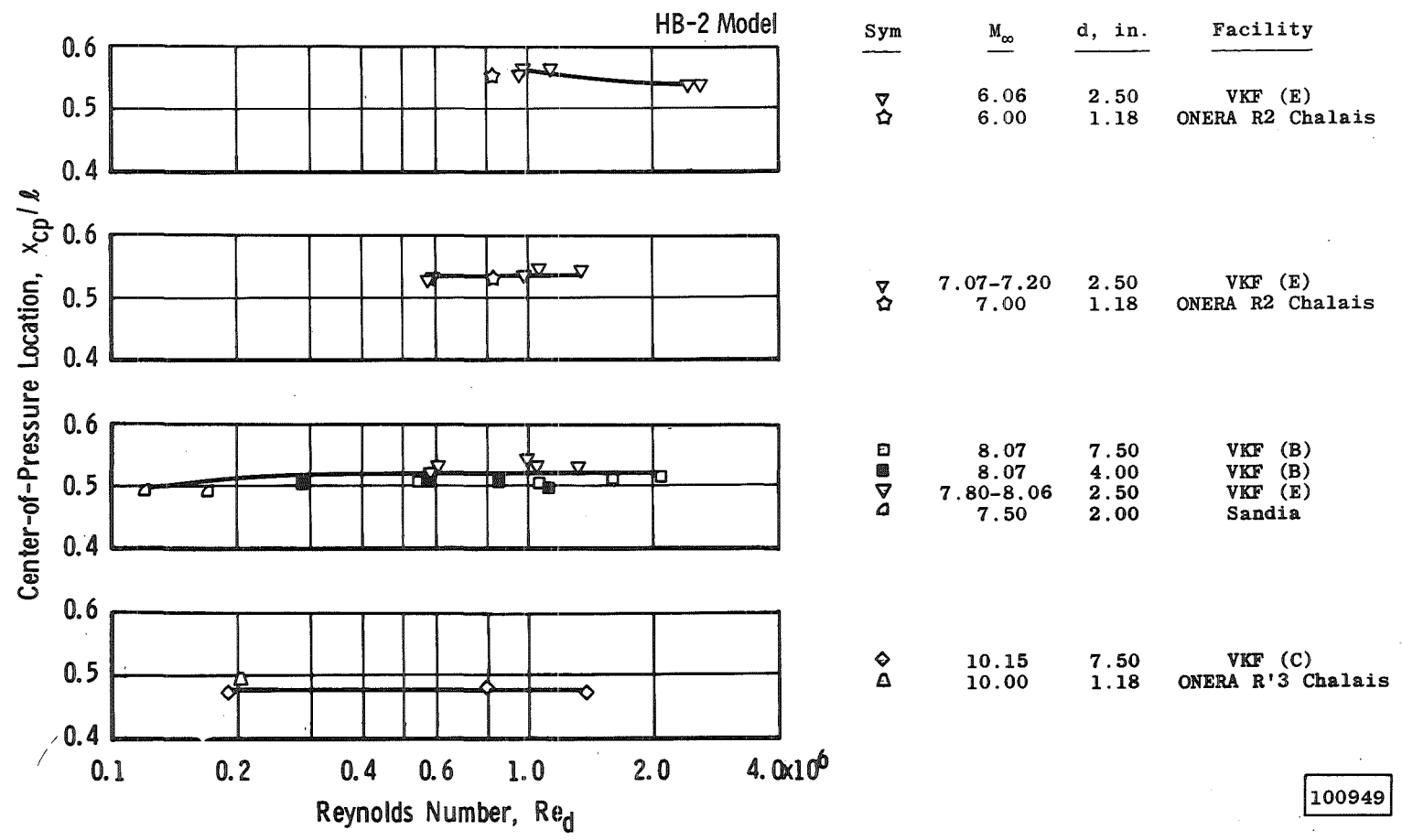
100949

b. Mach Numbers 6, 7, 8, and 10

Fig. 11 Concluded

HB-2 Model

Zero-Lift Forebody Axial-Force Coefficient, C_A

C_A 0.9, 0.8, 0.7

Pressure Integration

0.8, 0.8, 0.7, 0.6

0.7, 0.6, 0.5

Uncertainty Caused by Zero Shift at Max Re_d

0.7, 0.6, 0.5

Uncertainty Caused by Zero Shift at Max Re_d

0.7, 0.6, 0.5

0.1   0.2   0.4   0.6   1.0   2.0   4.0 x 10⁶

Reynolds Number, Re_d

Sym	M_∞	d, in.	Facility
O	1.50	4.00	VKF (A)
△	1.46	1.25	VKF (D)

Sym	M_∞	d, in.	Facility
O	2.00	4.00	VKF (A)
△	1.99	1.25	VKF (D)
☆	2.12	1.18	LRBA (C4)

Sym	M_∞	d, in.	Facility
O	3.00	4.00	VKF (A)
△	2.99	1.25	VKF (D)
☆	3.20	1.18	LRBA (C4)

Sym	M_∞	d, in.	Facility
O	4.02	4.00	VKF (A)
△	3.99	1.25	VKF (D)
☆	4.26	1.18	LRBA (C4)

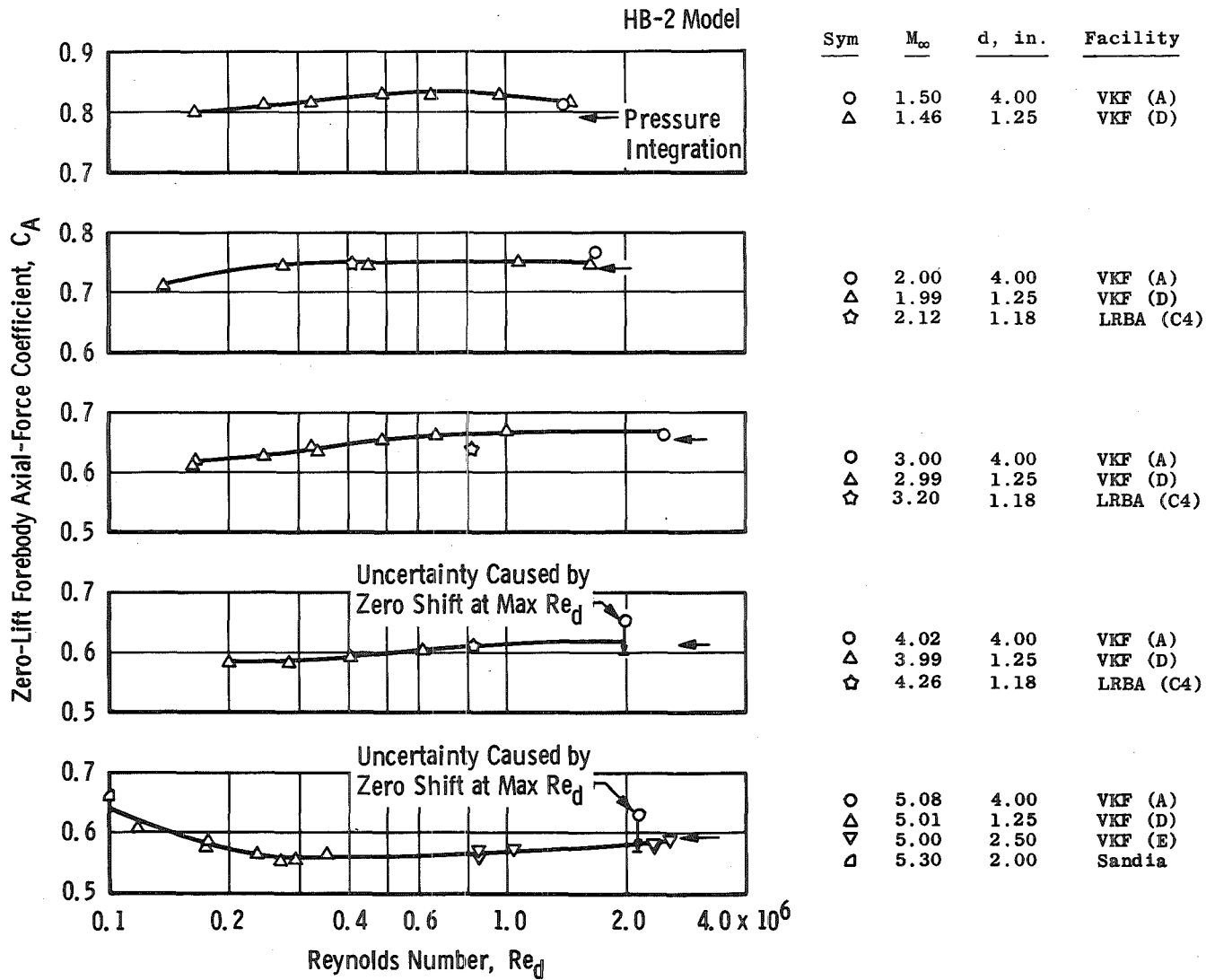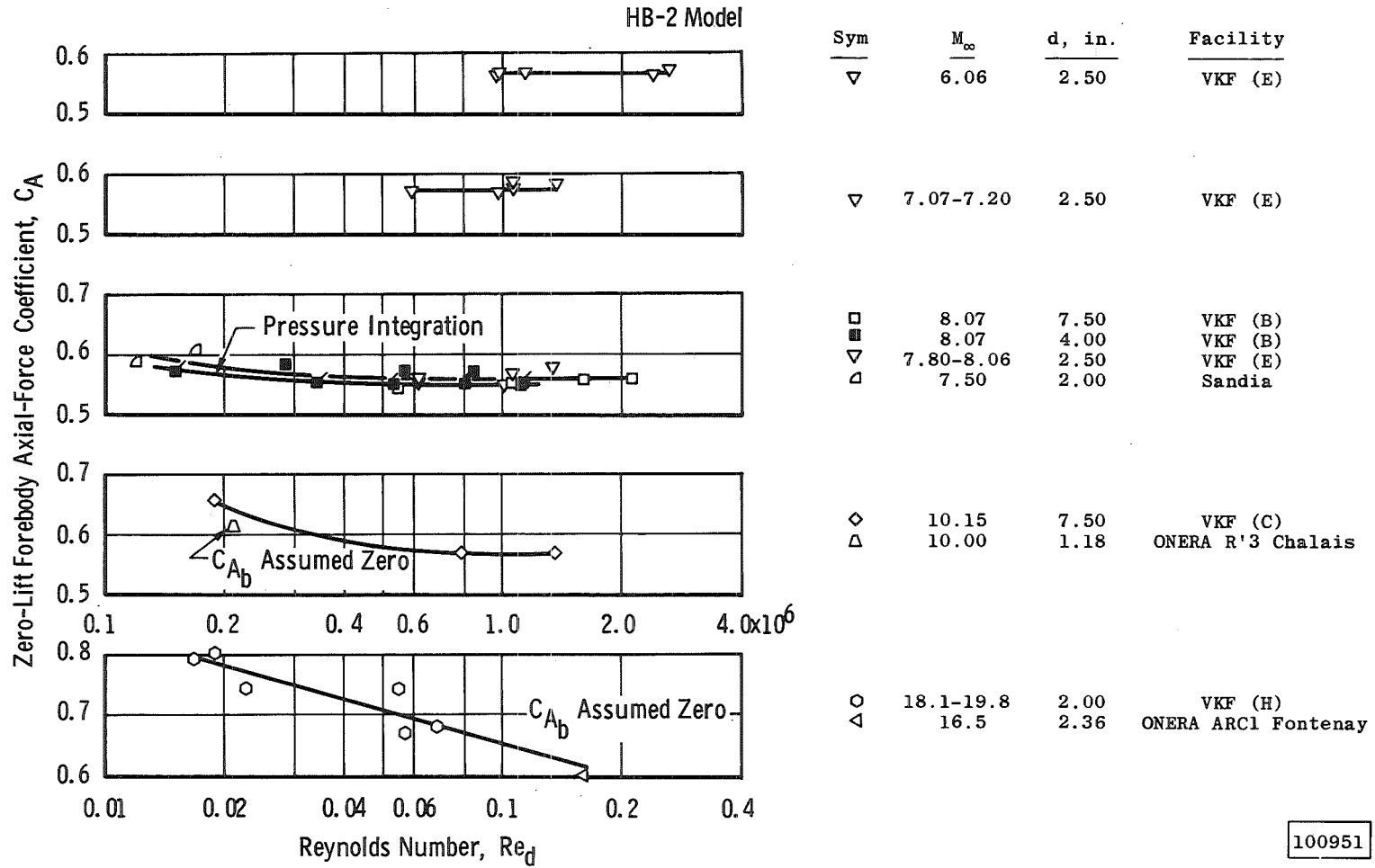| Sym	M_∞	d, in.	Facility
O	5.08	4.00	VKF (A)
△	5.01	1.25	VKF (D)
▽	5.00	2.50	VKF (E)
◿	5.30	2.00	Sandia

a. Mach Numbers 1.5, 2, 3, 4, and 5

Fig. 12 Zero-Lift Forebody Axial-Force Coefficient versus Reynolds Number for Model HB-2

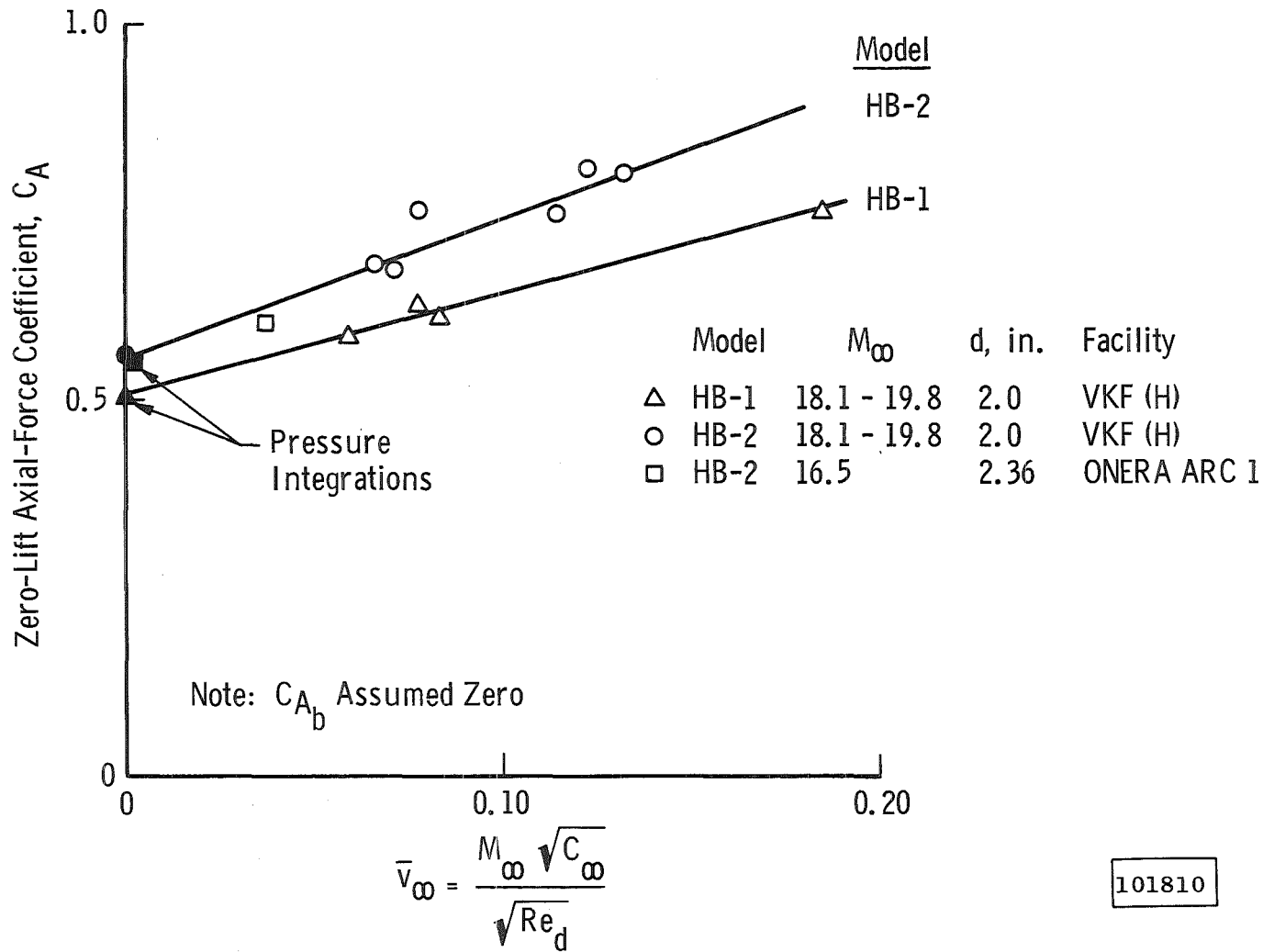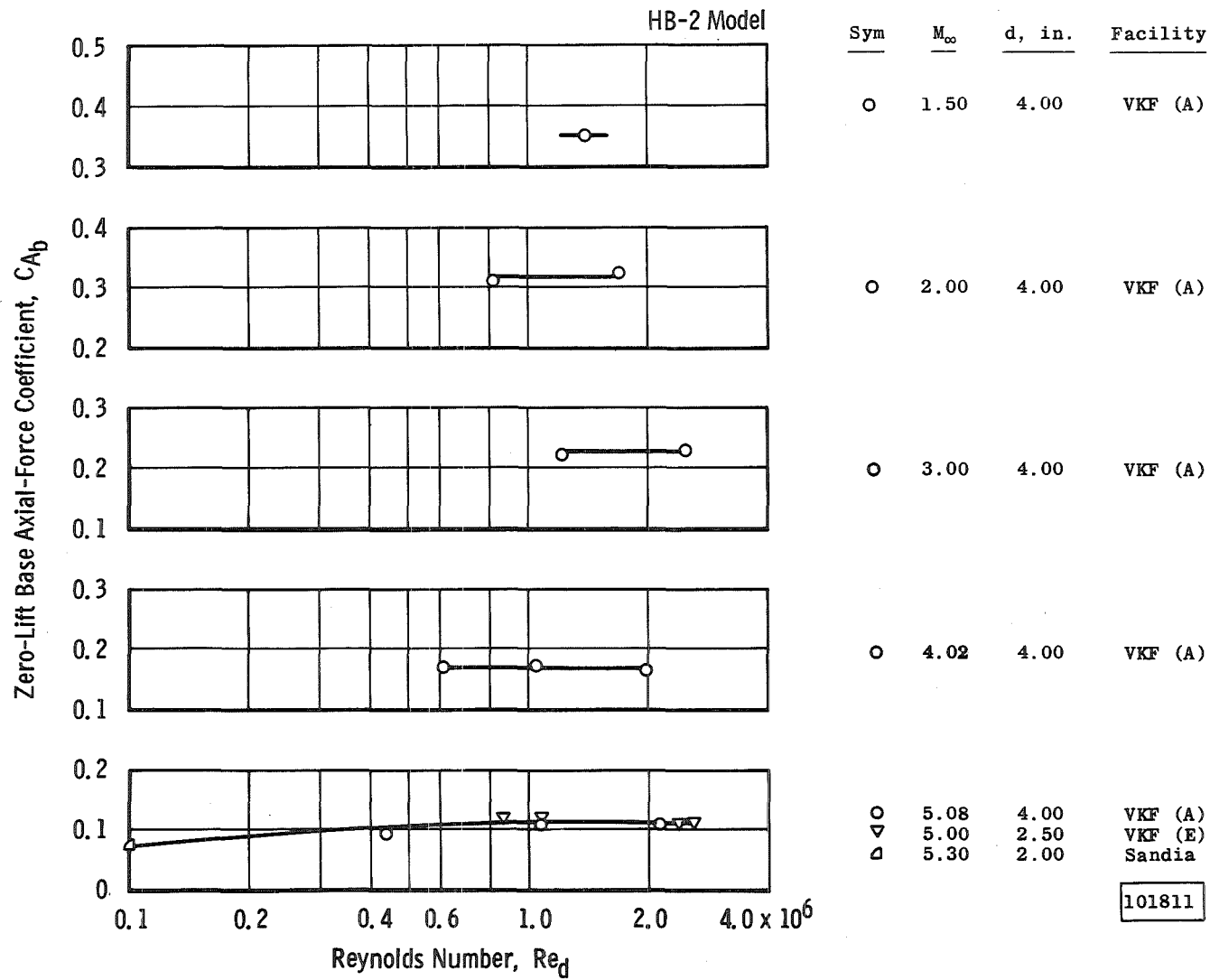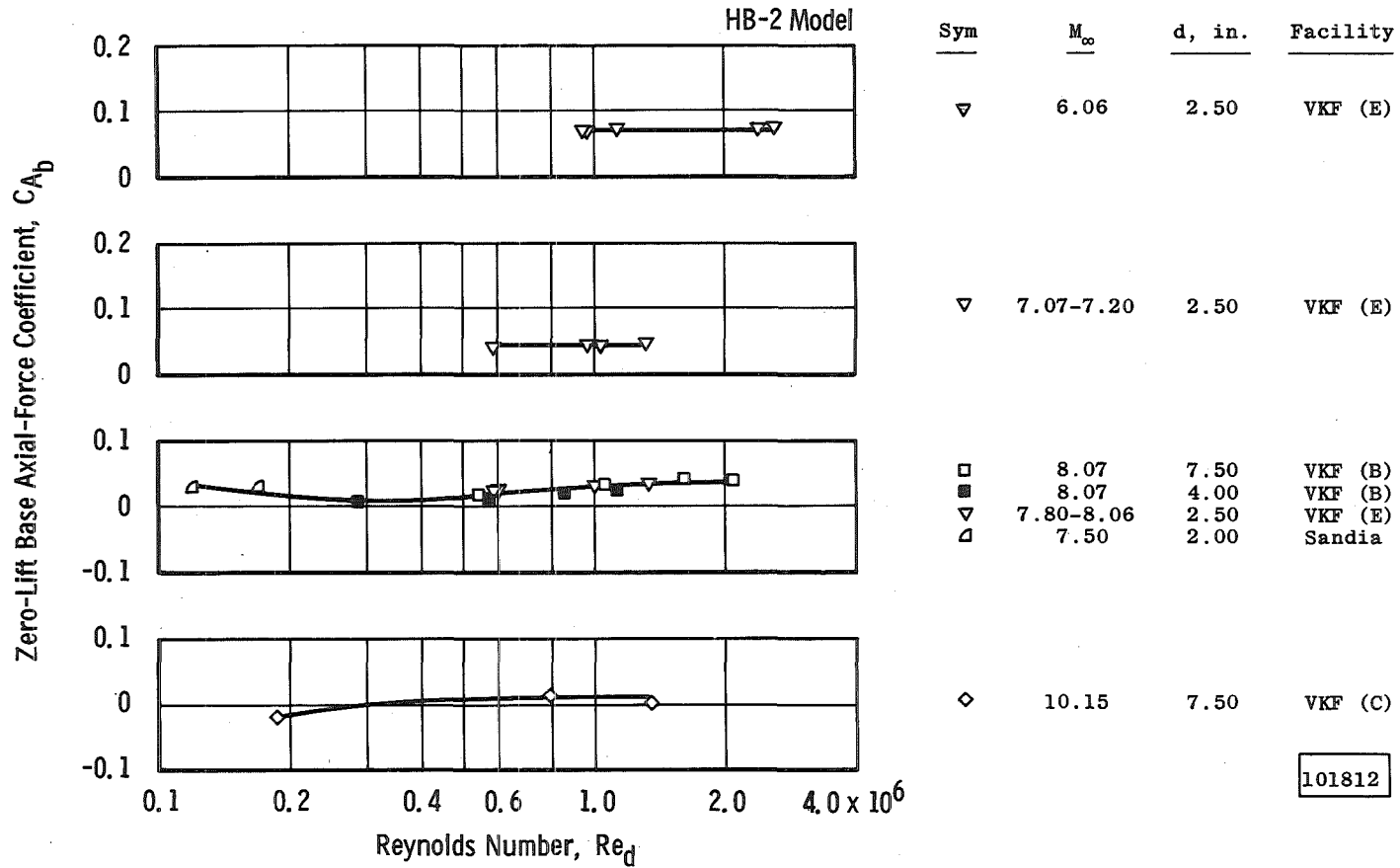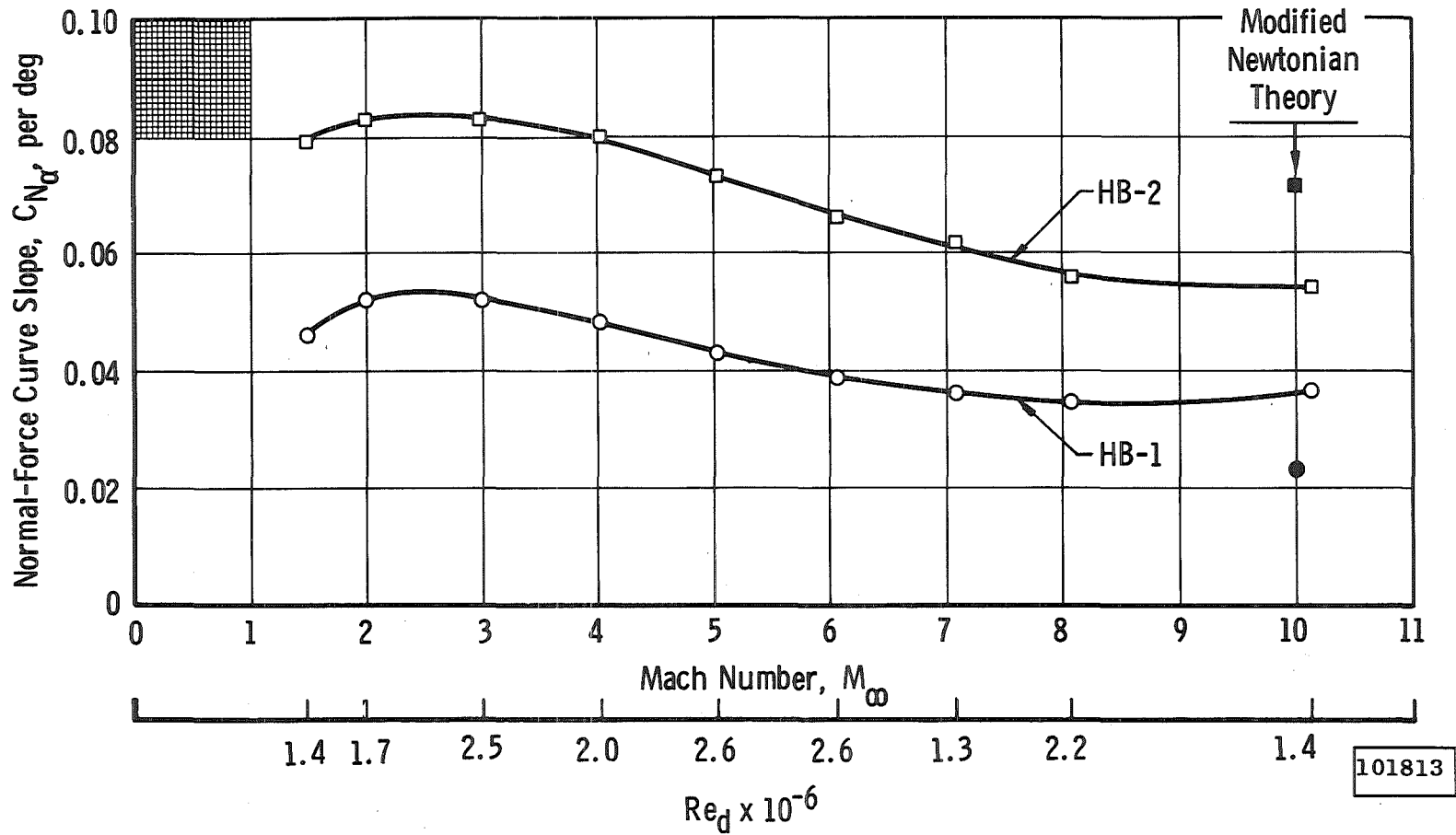b. Mach Numbers 6, 7, 8, 10, 16.5, and 20

Fig. 12 Concluded

Fig. 13 Zero-Lift Forebody Axial-Force Coefficient versus Viscous Interaction Parameter for Models HB-1 and HB-2

HB-2 Model

Sym	M_∞	d, in.	Facility
○	1.50	4.00	VKF (A)
○	2.00	4.00	VKF (A)
○	3.00	4.00	VKF (A)
○	4.02	4.00	VKF (A)
○	5.08	4.00	VKF (A)
▽	5.00	2.50	VKF (E)
△	5.30	2.00	Sandia

101811

Zero-Lift Base Axial-Force Coefficient, CA_b

Reynolds Number, Re_d

a. Mach Numbers 1.5, 2, 3, 4, and 5

Fig. 14 Zero-Lift Base Axial-Force Coefficient versus Reynolds Number for Model HB-2

HB-2 Model

Zero-Lift Base Axial-Force Coefficient, CA_b

Sym	M_∞	d, in.	Facility
▽	6.06	2.50	VKF (E)
▽	7.07-7.20	2.50	VKF (E)
□	8.07	7.50	VKF (B)
▣	8.07	4.00	VKF (B)
▽	7.80-8.06	2.50	VKF (E)
△	7.50	2.00	Sandia
◇	10.15	7.50	VKF (C)

101812

Reynolds Number, Re_d

b. Mach Numbers 6, 7, 8, and 10

Fig. 14 Concluded

Modified
Newtonian
Theory

HB-2

HB-1

0.10

0.08

0.06

0.04

0.02

0

Normal-Force Curve Slope, C_{N_α}, per deg

0   1   2   3   4   5   6   7   8   9   10   11

Mach Number, M_∞

1.4 1.7   2.5   2.0   2.6   2.6   1.3   2.2   1.4

$Re_d \times 10^{-6}$

101813

a. Initial Slope of Normal-Force Curve

Fig. 15 Comparison of Mach Number Effect on Models HB-1 and HB-2
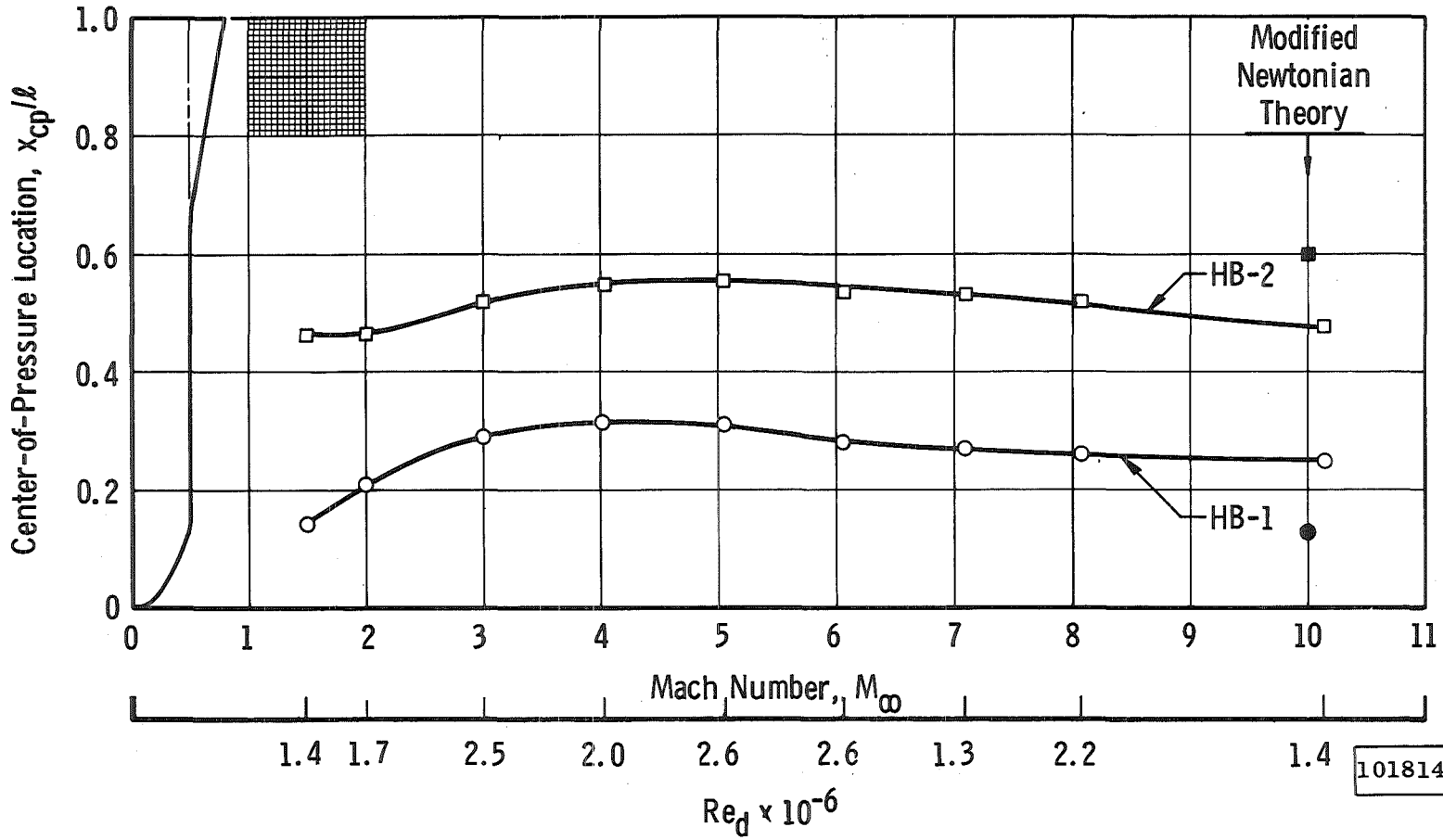
b. Center of Pressure

Fig. 15 Continued
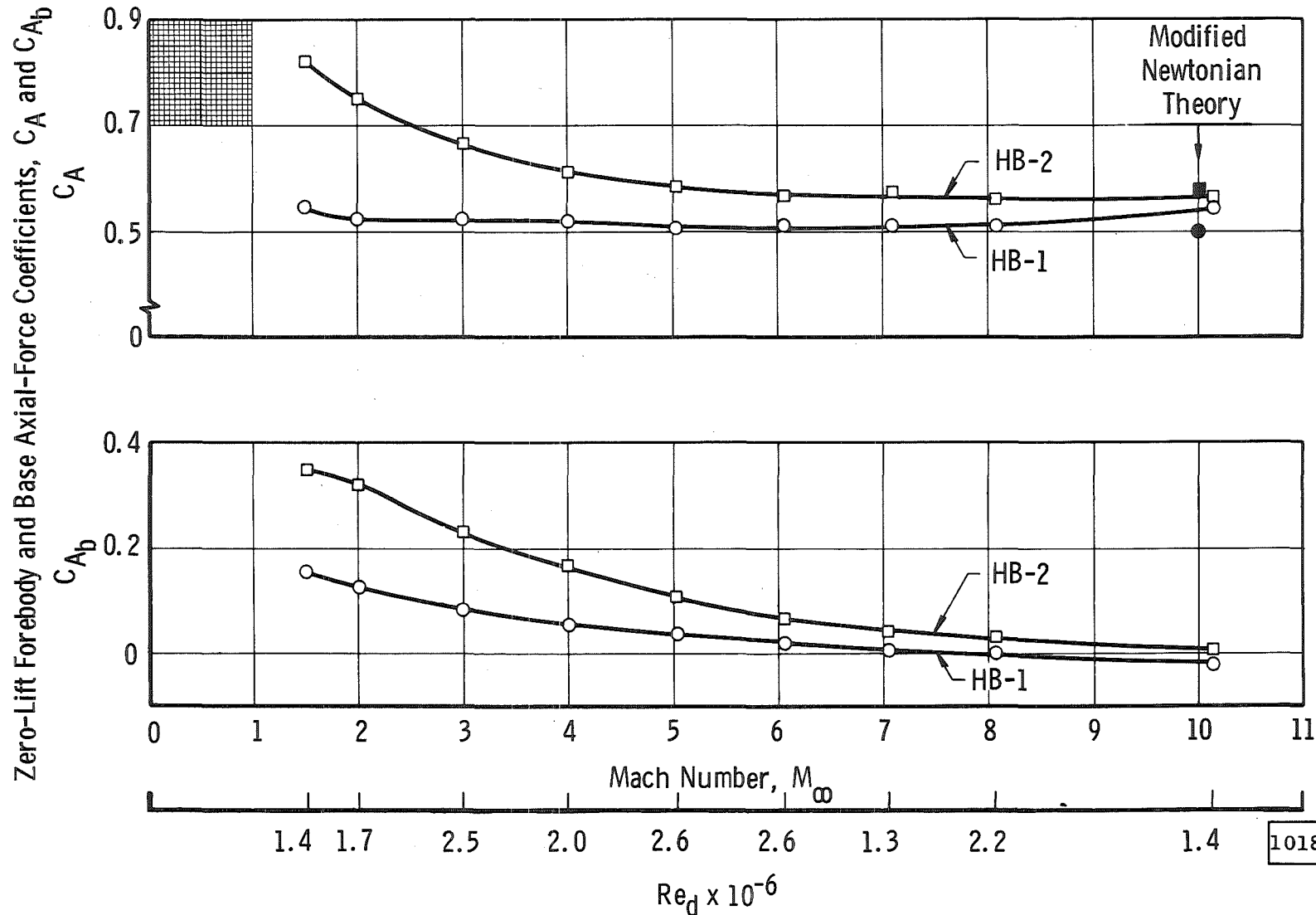
c. Zero-Lift Forebody and Base Axial-Force Coefficients

Fig. 15 Concluded
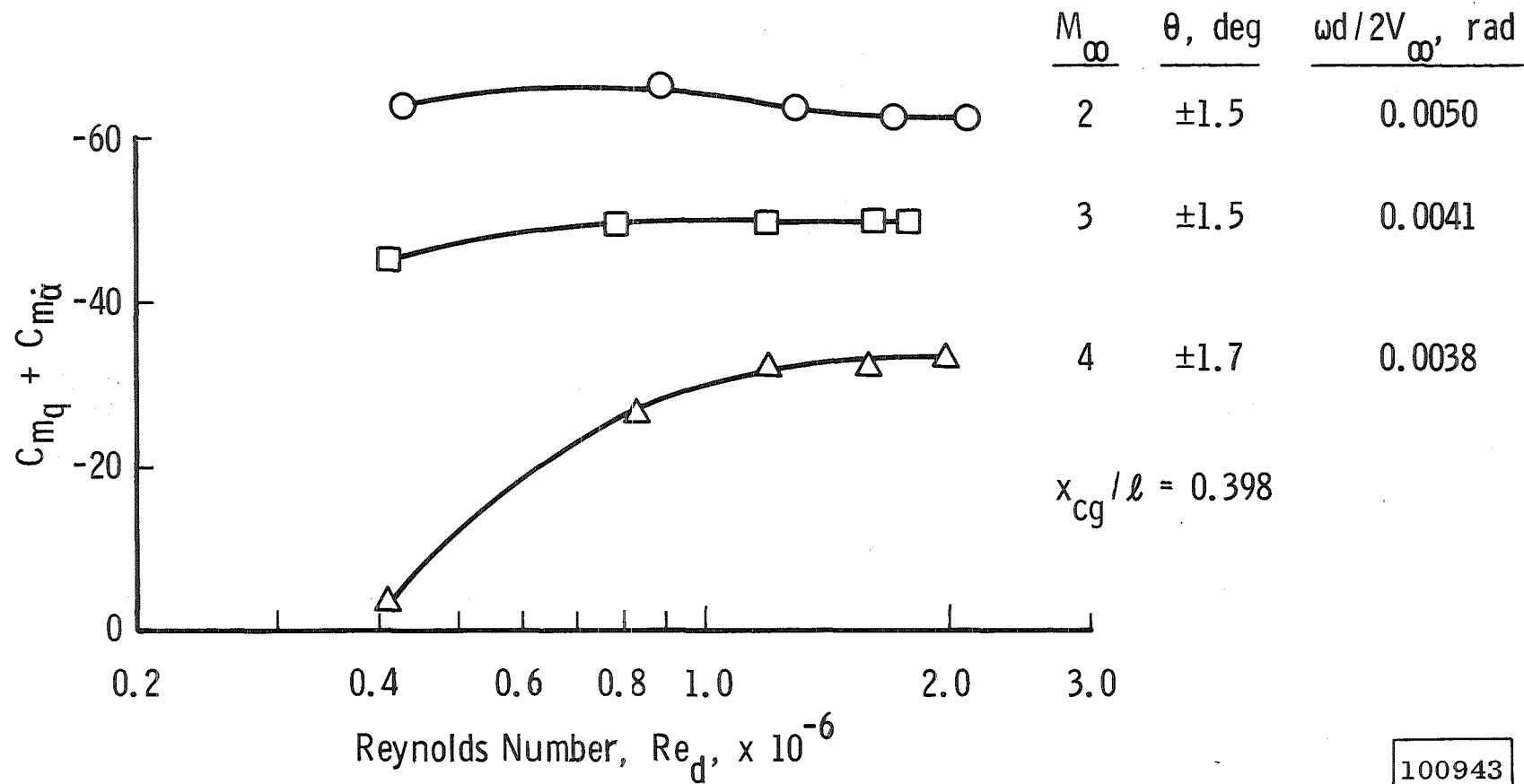
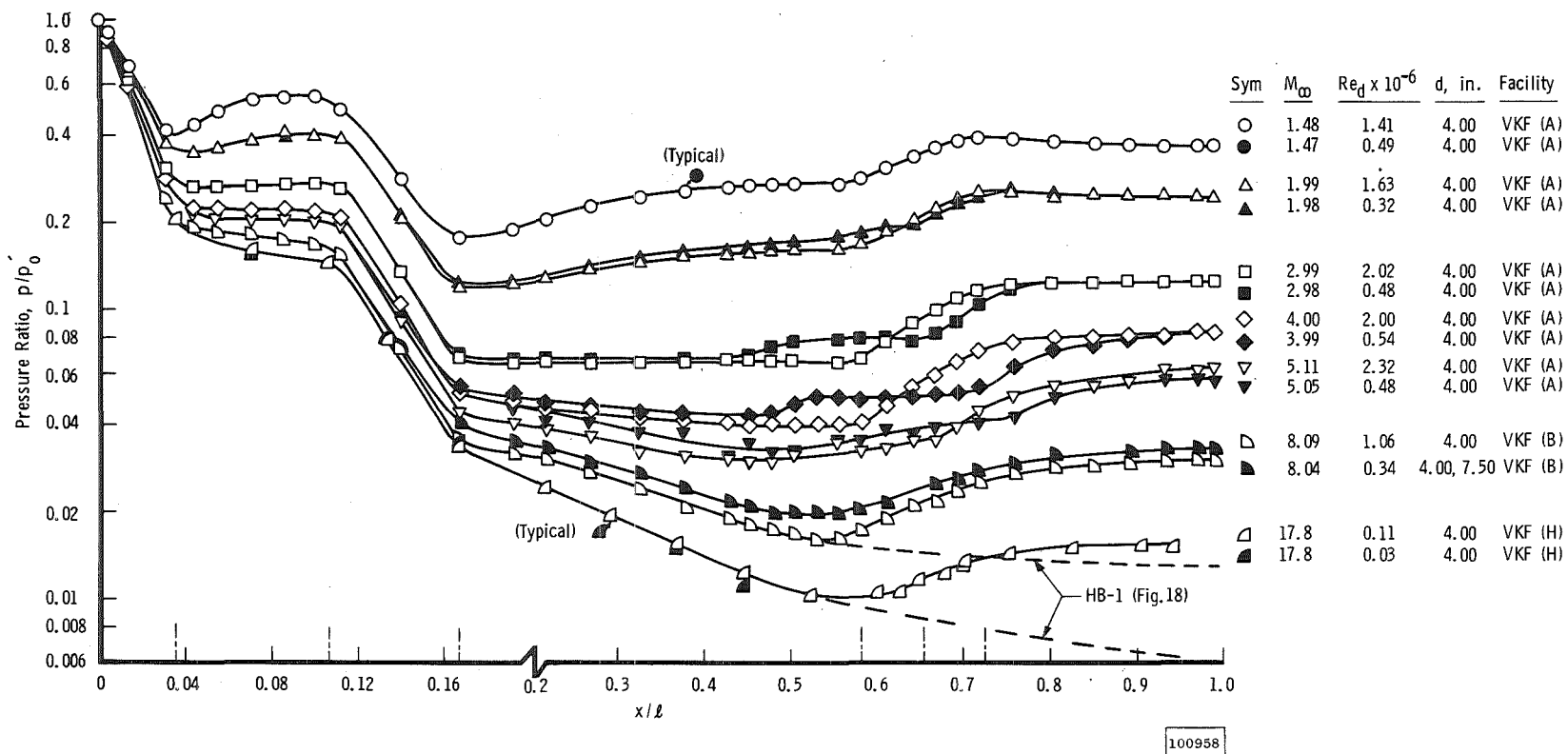Fig. 16 Damping-in-Pitch Derivatives versus Reynolds Number for Model HB-2 at Mach Numbers 2, 3, and 4

Fig. 17 Longitudinal Pressure Distributions at Zero Lift for Model HB-2 at Mach
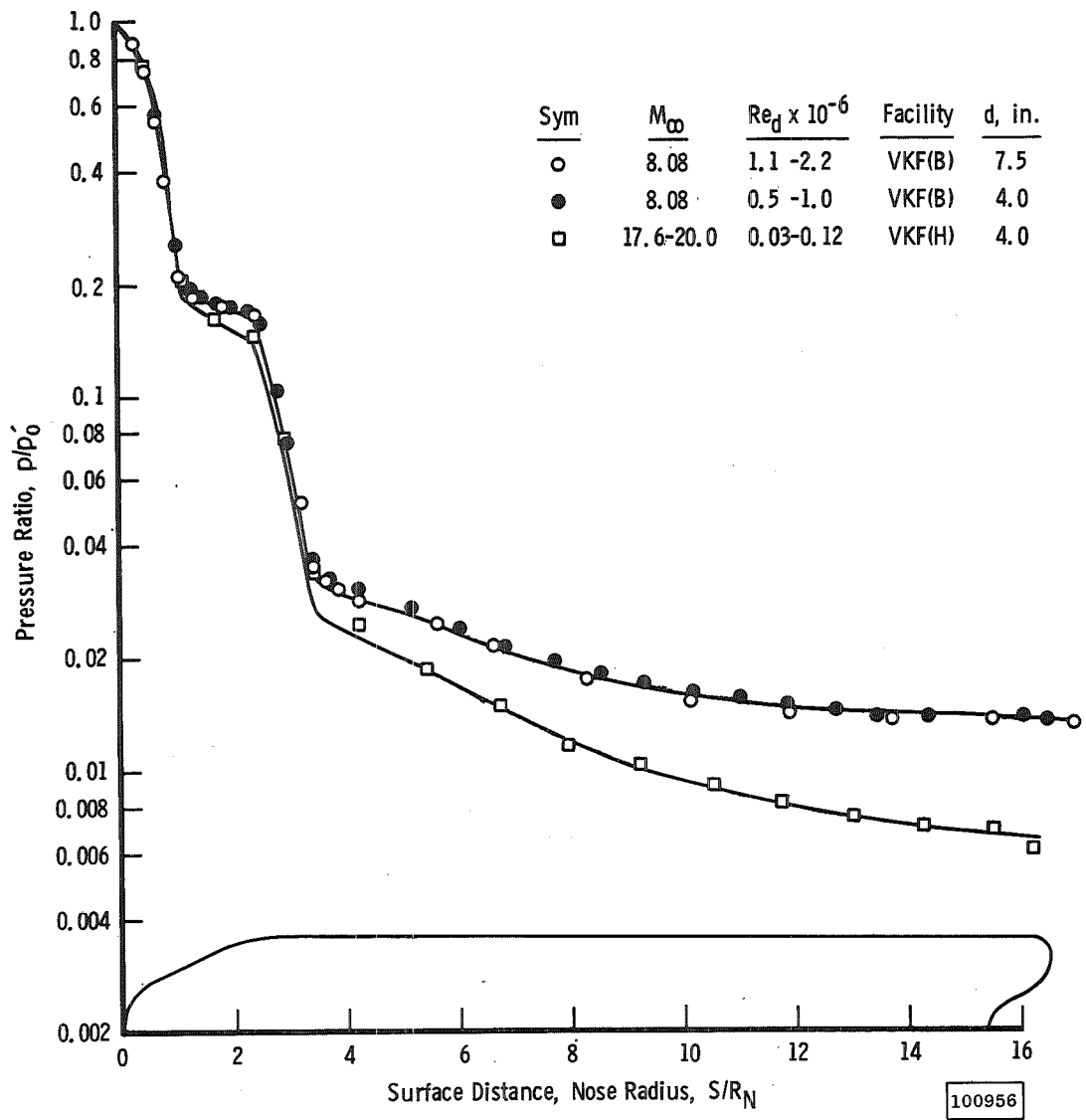Numbers 1.5, 2, 3, 4, 5, 8, and 18

Fig. 18 Longitudinal Pressure Distributions at Zero Lift for Model HB-1
at Mach Numbers 8 and 20

Pressure Ratio, p/p_0'

1.0
0.8
0.6

0.4

0.2

0.10
0.08

0.06

0.04

0.02

0.01

Fairing of VKF Data;
$M_\infty = 1.99$, $Re_d = 1.63 \times 10^6$

$M_\infty = 2.99$, $Re_d = 2.02 \times 10^6$

$M_\infty = 4.00$, $Re_d = 2.00 \times 10^6$
$M_\infty = 5.11$, $Re_d = 2.32 \times 10^6$
$M_\infty = 8.09$, $Re_d = 1.06 \times 10^6$
$M_\infty = 17.8$, $Re_d = 0.11 \times 10^6$

0   0.04   0.08   0.12   0.16   0.2   0.3   0.4   0.5   0.6   0.7   0.8   0.9   1.0

x/ℓ

100957

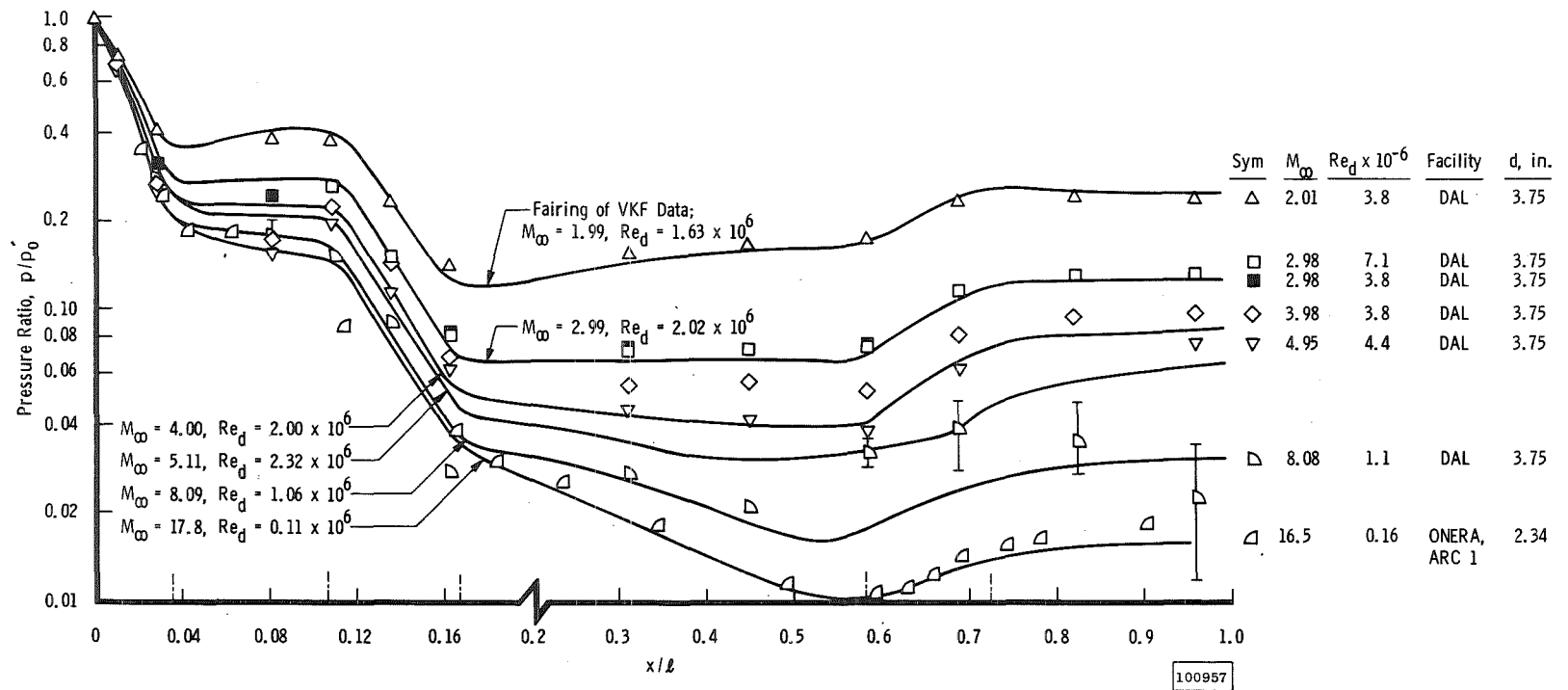| Sym	M_∞	$Re_d \times 10^{-6}$	Facility	d, in.
△	2.01	3.8	DAL	3.75
□	2.98	7.1	DAL	3.75
■	2.98	3.8	DAL	3.75
◇	3.98	3.8	DAL	3.75
▽	4.95	4.4	DAL	3.75
◁	8.08	1.1	DAL	3.75
◁	16.5	0.16	ONERA, ARC 1	2.34

Fig. 19 Comparison of Longitudinal Pressure Distributions at Zero Lift for Model HB-2 from VKF, DAL, and ONERA
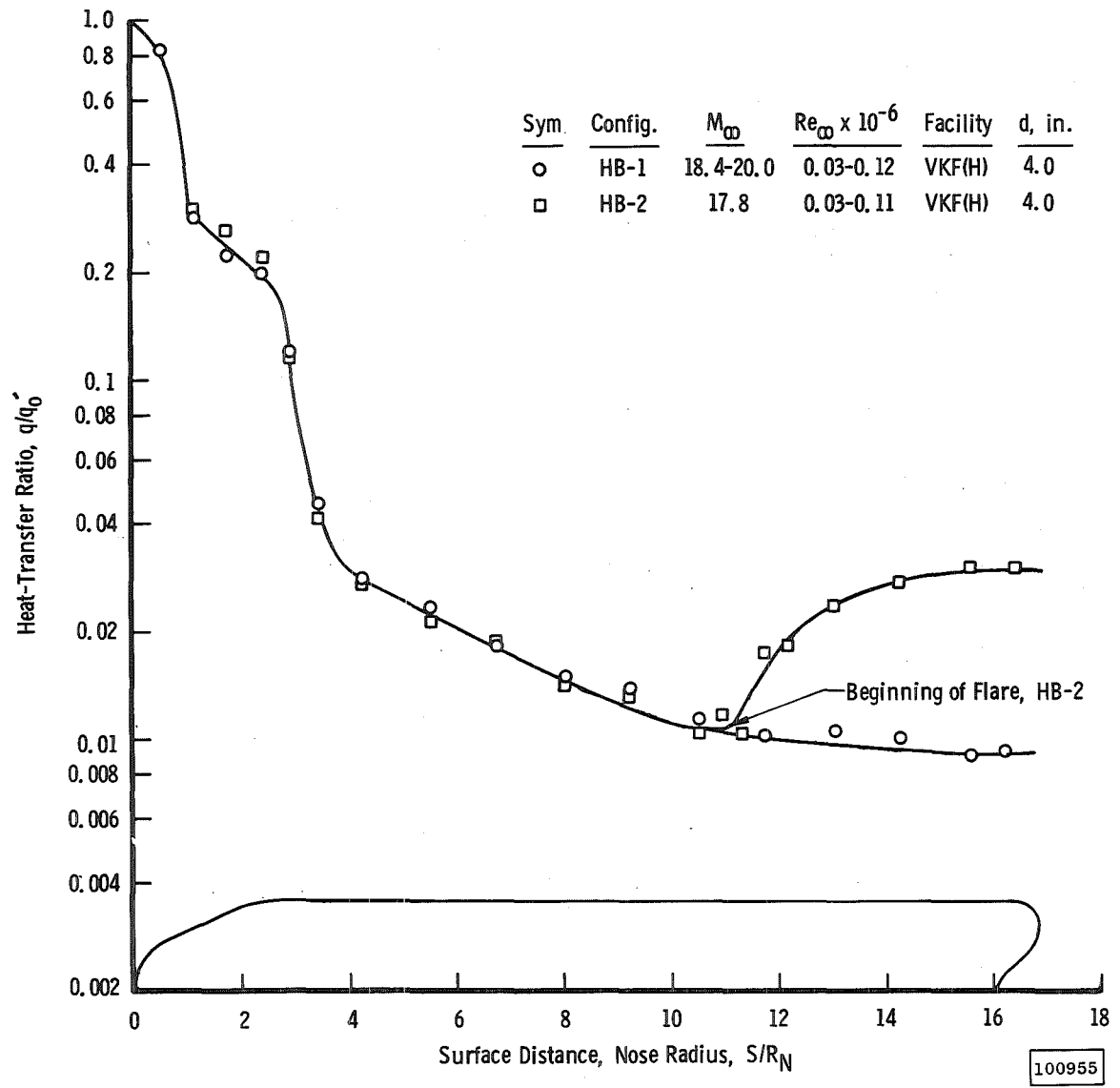
Fig. 20 Longitudinal Heat-Transfer Distribution at Zero Lift for Models HB-1
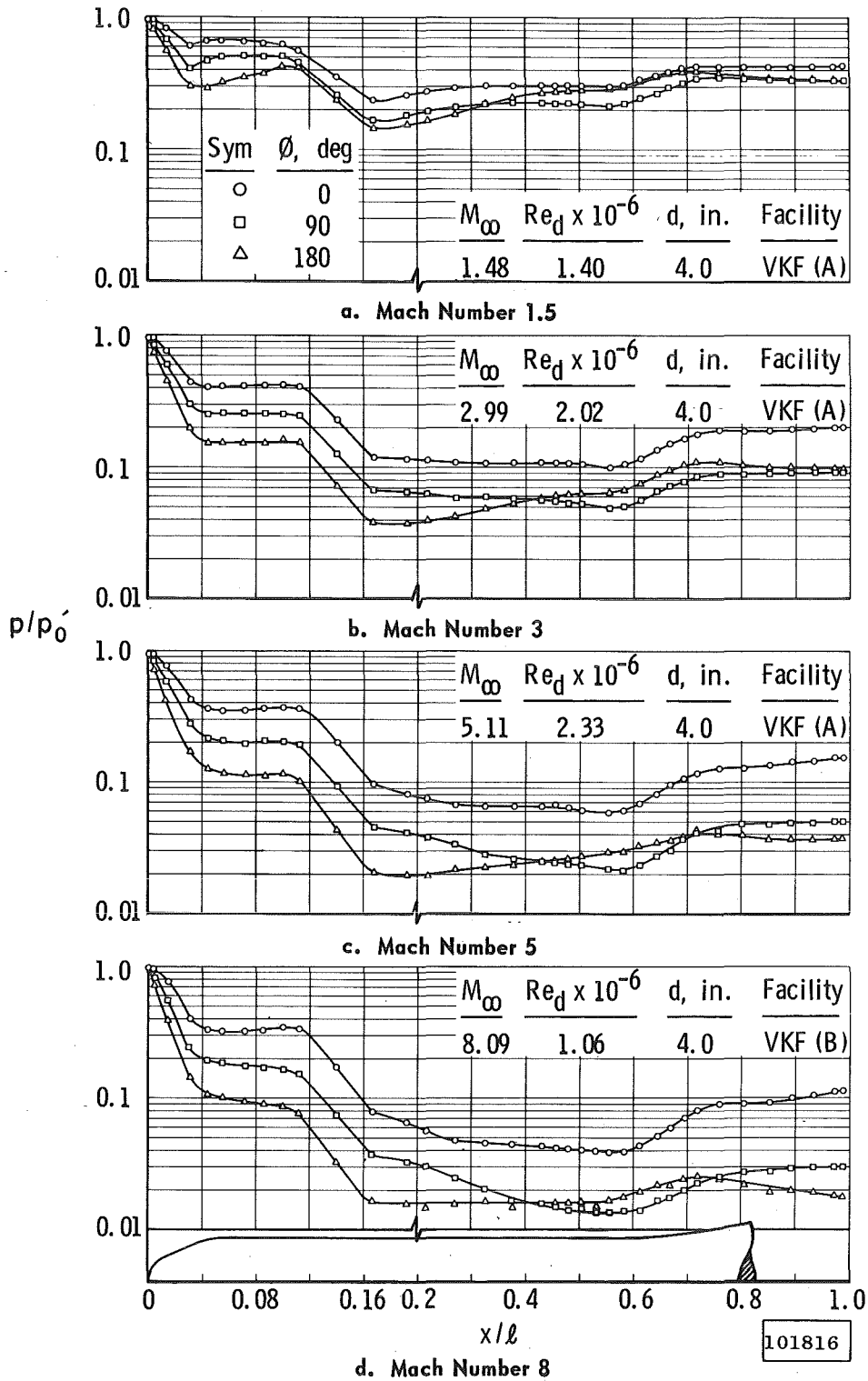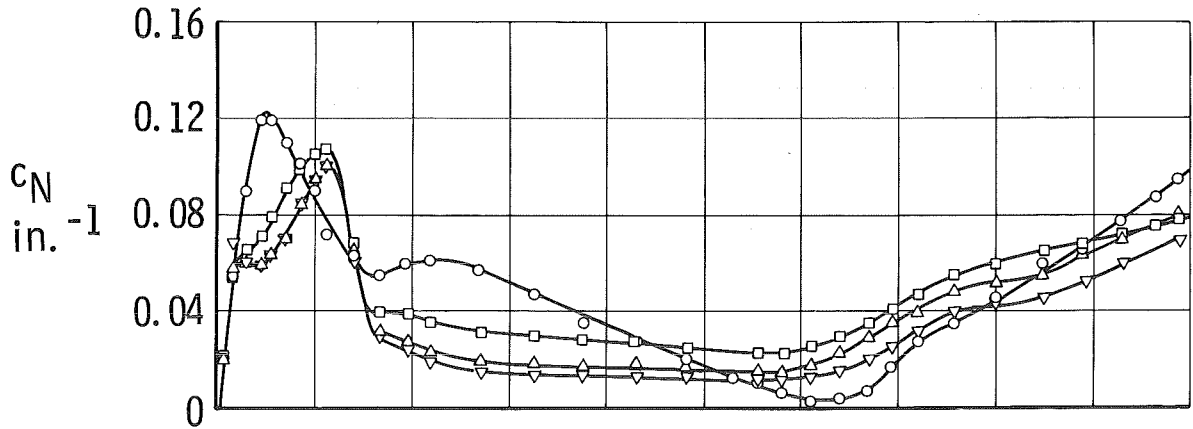and HB-2 at Mach 18

100955

a. Mach Number 1.5

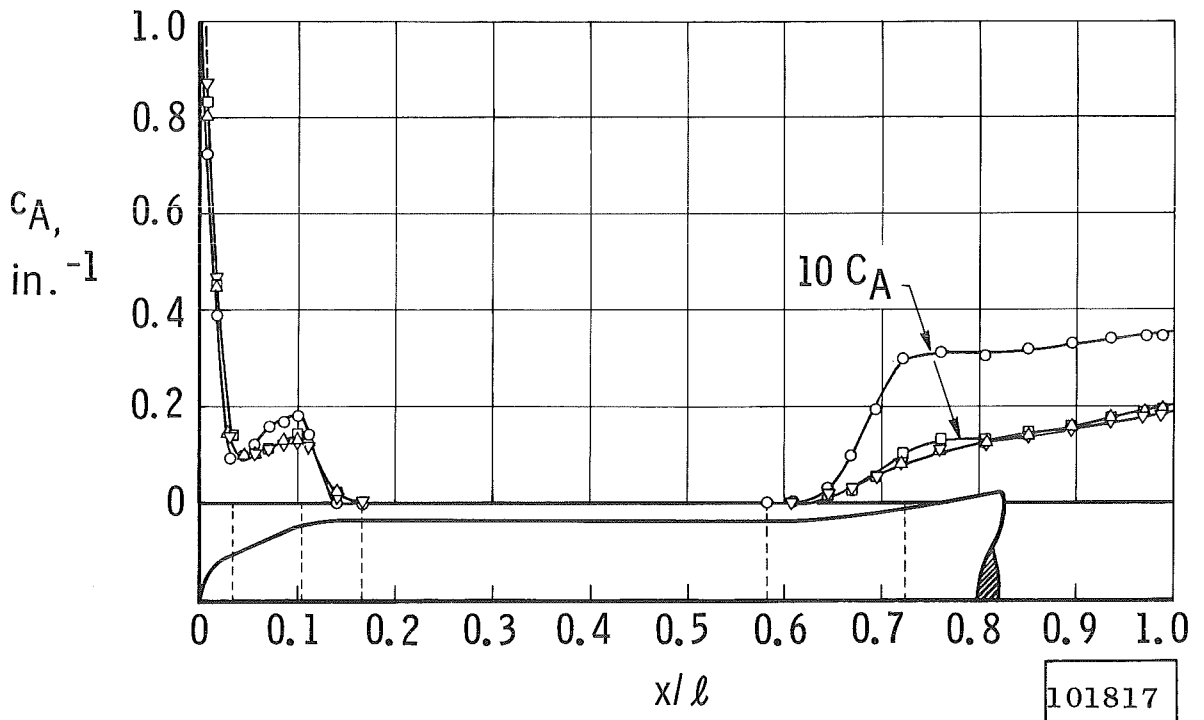b. Mach Number 3

c. Mach Number 5

d. Mach Number 8

Fig. 21 Longitudinal Pressure Distributions for an Angle of Attack of 10 deg
at Three Circumferential Positions for Model HB-2

Sym	M_∞	$Re_d \times 10^{-6}$	d, in.	Facility
○	1.48	1.40	4.0	VKF (A)
□	2.99	2.02	''	VKF (A)
△	5.11	2.33	''	VKF (A)
▽	8.09	1.06	''	VKF (B)

a. Local Normal-Force Coefficient Distribution

b. Local Axial-Force Coefficient Distribution

Fig. 22 Local Normal-Force and Axial-Force Coefficient Distributions on Model HB-2 at an Angle of Attack of 10 deg for Mach Numbers 1.5, 3, 5, and 8